Chapter 19.6. Electron cryomicroscopy of biological macromolecules

T. S. Baker and R. Henderson

19.6.1. Abbreviations used

0D	Zero-dimensional (single particles)
1D	One-dimensional (helical)
2D	Two-dimensional
3D	Three-dimensional
EM	Electron microscope/microscopy
CryoTEM	Transmission electron cryomicroscopy
FEG	Field-emission gun
CTF	Contrast-transfer function
MTF	Modulation transfer function
DQE	Detective quantum efficiency
DPR	Differential phase residual
FSC	Fourier shell correlation
CCD	Charge-coupled device (slow-scan TV detector)

19.6.2. Introduction: macromolecular structure determination using electron microscopy

The two principal methods of macromolecular structure determination that use scattering techniques are electron microscopy and X-ray crystallography. The most important difference between the two is that the scattering cross section is about 10^5 times greater for electrons than it is for X-rays, so significant scattering using electrons is obtained for specimens that are 1 to 10 nm thick, whereas scattering or absorption of a similar fraction of an illuminating X-ray beam requires crystals that are 100 to 500 μm thick, though in recent years smaller crystals, still > 1 μm thick, have become usable at synchrotron sources. The second main difference is that electrons are much more easily focused than X-rays since they are charged particles that can be deflected by electric or magnetic fields. As a result, electron lenses are much superior to X-ray lenses and can be used to produce a magnified image of an object as easily as a diffraction pattern. This allows the electron microscope to be switched back and forth instantly between imaging and diffraction modes so that the image of a single molecule at any magnification can be obtained as conveniently as the electron-diffraction pattern of a thin crystal.

In the early years of electron microscopy of macromolecules, electron micrographs of molecules embedded in a thin film of heavy-atom stains (Brenner & Horne, 1959; Huxley & Zubay, 1960) were used to produce pictures which were interpreted directly. Beginning with the work of Klug (Klug & Berger, 1964), a more rigorous approach to image analysis led first to the interpretation of the two-dimensional (2D) images as the projected density summed along the direction of view and then to the ability to reconstruct the three-dimensional (3D) object from which the images arose (DeRosier & Klug, 1968; Hoppe *et al.*, 1968), with subsequent more sophisticated treatment of image contrast transfer (Erickson & Klug, 1971).

Later, macromolecules were examined by electron diffraction and imaging without the use of heavy-atom stains by embedding the specimens in either a thin film of glucose (Unwin & Henderson, 1975) or in a thin film of rapidly frozen water (Taylor & Glaeser, 1974; Dubochet *et al.*, 1982, 1988), which required the specimen to be cooled while it was examined in the electron microscope. This use of unstained specimens thus led to the structure determination of the molecules themselves, rather than the structure of a 'negative stain' excluding volume, and has created the burgeoning field of 3D electron microscopy of macromolecules.

Many medium-resolution (*i.e.*, 5–15 Å) structures of macromolecular assemblies (*e.g.* ribosomes), spherical and helical viruses, and larger protein molecules have now been determined by transmission electron cryomicroscopy (cryoTEM) in ice. A small number of atomic resolution structures have been obtained by cryoTEM of thin 2D crystals embedded in glucose, trehalose or tannic acid (Henderson *et al.*, 1990; Kühlbrandt *et al.*, 1994; Nogales *et al.*, 1998; Murata *et al.*, 2000; Gonen *et al.*, 2005; Holm *et al.*, 2006), where specimen cooling reduced the effect of radiation damage. One of these, the structure of bacteriorhodopsin (Henderson *et al.*, 1990) provided the first structure of a seven-helix membrane protein, and recent studies, particularly on aquaporins, are providing detailed insights into lipid–protein interactions (Reichow & Gonen, 2009). During the last few years, two different helical structures have allowed atomic models to be constructed from images of ice-embedded specimens (Miyazawa *et al.*, 2003; Yonekura, Maki-Yonekura & Namba, 2003) and the resolution of the best icosahedral structures has likewise improved dramatically to yield atomic models (*e.g.* Jiang *et al.*, 2008; Yu, Jin & Zhou, 2008; Zhang *et al.*, 2008; Chen *et al.*, 2009). Medium-resolution density distributions can often be interpreted in terms of the chemistry of the structure if a high-resolution model of one or more of the component pieces has already been obtained by X-ray, electron microscopy or NMR methods. As a result, the use of electron microscopy is becoming a powerful technique for which, in some cases, no alternative approach is possible. Numerous useful reviews (*e.g.* Amos *et al.*, 1982; Dubochet *et al.*, 1988; Baker *et al.*, 1999; van Heel *et al.*, 2000; Frank, 2002; Henderson, 2004; Chiu *et al.*, 2005) and books (Frank, 2006*b*; Glaeser *et al.*, 2007) have been written.

19.6.3. Physics of electron scattering and radiation damage

A schematic overview of scattering and imaging in the electron microscope is depicted in Fig. 19.6.3.1. The incident electron beam passes through the specimen and individual electrons are either unscattered or scattered by the atoms of the specimen. This scattering occurs either elastically, with no loss of energy and therefore no energy deposition in the specimen, or inelastically, with consequent energy loss by the scattered electron and accompanying energy deposition in the specimen, resulting in radiation damage. The electrons emerging from the specimen are then collected by the imaging optics, shown here for simplicity as a single lens, but in practice consisting of a complex system of five or six lenses with intermediate images being produced at successively higher magnification at different positions down the column. Finally, in the viewing area, either the electron-

diffraction pattern or the image can be seen directly by eye on the phosphor screen, or detected by a TV or CCD camera, or recorded on photographic film.

In practice, the electron flux through the specimen is relatively low, so that only one electron at a time is in the column interacting with the specimen. This means that the unscattered and elastically scattered beams are in reality quantum-mechanical wavefronts, in which a wave function describes the probability distribution until the electron is actually recorded in the detector or on film. Where an inelastic event results in energy deposition and accompanying radiation damage in the specimen, the path of that electron, as well as its energy, wavelength and probability distribution, are slightly altered and this degrades the image.

19.6.3.1. Elastic and inelastic scattering

The coherent, elastically scattered electrons contain the high-resolution information describing the structure of the specimen. The amplitudes and phases of the scattered electron beams are directly related to the amplitudes and phases of the Fourier components of the atomic distribution in the specimen. When the
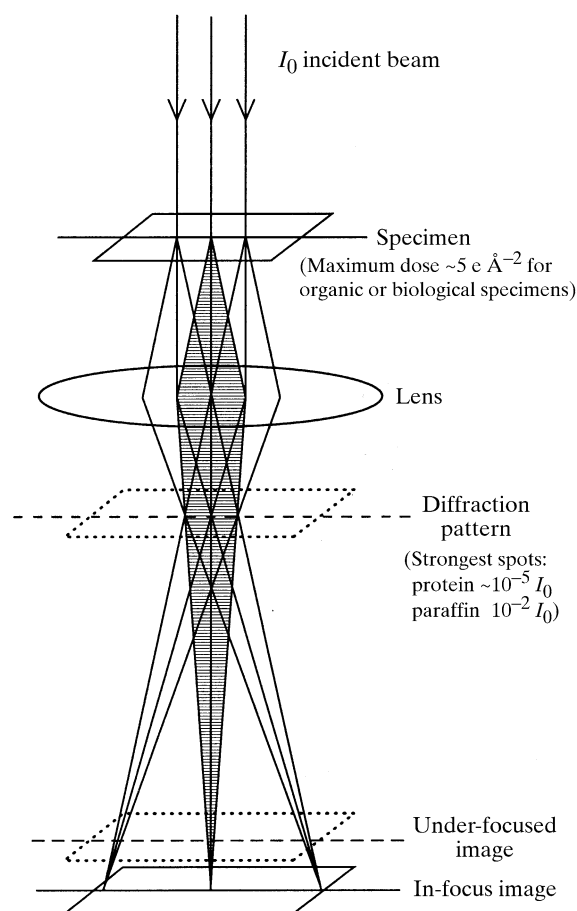
Figure 19.6.3.1
Schematic diagram showing the principle of image formation and diffraction in the transmission electron microscope. The incident beam, I_0, illuminates the specimen. Scattered and unscattered electrons are collected by the objective lens and focused back to form first an electron-diffraction pattern and then an image. For a 2D or 3D crystal, the electron-diffraction pattern would show a lattice of spots, each of whose intensity is a small fraction of that of the incident beam. In practice, an in-focus image has virtually no contrast, so images are recorded with the objective lens underfocused to take advantage of the out-of-focus phase-contrast mechanism. Higher electron doses than indicated can be used at lower resolution. The given dose of 5 e Å^{-2} applies for high-resolution (~4 Å) structural features.

scattered beams are recombined with the unscattered beam in the image, they create an interference pattern (the image) which, for thin specimens, is related approximately linearly to the density variations in the specimen. Information about the structure of the specimen can then be retrieved by digitization and computer-based image processing, as described in Section 19.6.5. The elastic scattering cross sections for electrons are not as simply related to the atomic composition as happens with X-rays. With X-ray diffraction, the scattering factors are simply proportional to the number of electrons in each atom, normally equal to the atomic number. Since elastically scattered electrons are in effect diffracted by the electrical potential inside atoms, the scattering factor for electrons depends not only on the nuclear charge but also on the size of the surrounding electron cloud, which screens the nuclear charge. As a result, electron scattering factors in the resolution range of interest in macromolecular structure determination (up to $\frac{1}{3}$ Å^{-1}) are very sensitive to the effective radius of the outer valency electrons and therefore depend sensitively on the chemistry of bonding. Although this is a fascinating field in itself with interesting work already carried out by the gas-phase electron-diffraction community (*e.g.* Hargittai & Hargittai, 1988), it is still an area where much work remains to be done. At present, it is probably adequate to think of the density obtained in macromolecular structure analysis by electron microscopy as roughly equivalent to the electron density obtained by X-ray diffraction but with the contribution from hydrogen atoms being somewhat greater relative to carbon, nitrogen and oxygen.

Those electrons that are inelastically scattered lose energy to the specimen by a number of mechanisms. The energy-loss spectrum for a typical biological specimen is dominated by the large cross section for plasmon scattering in the energy range 20–30 eV with a continuum in the distribution which decreases up to higher energies. At discrete high energies, specific inner electrons in the K shell of carbon, nitrogen or oxygen can be ejected with corresponding peaks in the energy-loss spectrum appearing at 200–400 eV. Any of these inelastic interactions produces a deviation in the direction of the scattered electron and, as a result, the resolution of any information present in the energy-loss electron signal is reduced. Chromatic aberration in the objective lens results in these inelastic electrons contributing to the image only at relatively low resolution, around 15 Å (Isaacson *et al.*, 1974). Consequently, the inelastically scattered electrons are generally considered to contribute little, except noise, to the images. In the future, once electron cryo-microscopes with chromatic aberration correctors become available (expected by 2012), one may be able to obtain improved energy-loss images. Chromatic-aberration-corrected electron microscopes are already available for materials science (Kabius *et al.*, 2009).

19.6.3.2. Radiation damage

The most important consequence of inelastic scattering is the deposition of energy into the specimen. This is initially transferred to secondary electrons, which have an average energy (20 eV) that is five or ten times greater than the valence bond energies. These secondary electrons interact with other components of the specimen and produce numerous reactive chemical species, including free radicals. In ice-embedded samples, these would be predominantly highly reactive hydroxyl free radicals that arise from the frozen water molecules. In turn, these react with the embedded macromolecules and create a great variety of radiation products such as modified side chains, cleaved poly-

peptide backbones and a host of molecular fragments. From radiation-chemistry studies, it is known that thiol or disulfide groups react more quickly than aliphatic groups and that aromatic groups, including nucleic acid bases, are the most resistant (Burmeister, 2000; Weik *et al.*, 2000; Meents *et al.*, 2010). Nevertheless, the end effect of the inelastic scattering is the degradation of the specimen to produce a cascade of hetero-geneous products, some of which resemble the starting structure more closely than others. Some of the secondary electrons also escape from the surface of the specimen, causing it to charge up during the exposure. As a rough rule, for 100 kV electrons the dose that can be used to produce an image in which the starting structure at high resolution is still recognizable is about 1 e Å^{-2} for organic or biological materials at room temperature, 5 e Å^{-2} for a specimen near liquid-nitrogen temperature ($-170\,^{\circ}\text{C}$) and 10 e Å^{-2} for a specimen near liquid-helium temperature (4–8 K). However, individual experimenters will often exceed these doses if they wish to enhance the low-resolution information in the images, which is less sensitive to radiation damage. The effects of radiation damage owing to electron irradiation are essentially identical to those from X-ray or neutron irradiation for biological macromolecules except for the amount of energy deposition per useful coherent elastically scattered event (Henderson, 1995). For electrons scattered by biological structures at all electron energies of interest, the number of inelastic events exceeds the number of elastic events by a factor of three to four, so that 60 to 80 eV of energy is deposited for each elastically scattered electron. This limits the amount of information in an image of a single biological macromolecule. Consequently, the 3D atomic structure cannot be determined from a single molecule but requires the averaging of the information from a few thousand molecules in theory, and even more in practice (Henderson, 1995; Rosenthal & Henderson, 2003; Glaeser, 2008*b*; Cheng & Walz, 2009). Crystals used for X-ray or neutron diffraction contain many orders of magnitude more molecules.

It is possible to collect both the elastically and the inelastically scattered electrons simultaneously with an energy analyser and, if a fine electron beam is scanned over the specimen, then a scanning transmission electron micrograph displaying different properties of the specimen can be obtained (*e.g.* Tichelaar *et al.*, 1980; Crewe, 1983; Muller *et al.*, 2008). Alternatively, conventional transmission electron microscopes to which an energy filter has been added can be used to select out a certain energy band of the electrons from the image (*e.g.* Yonekura *et al.*, 2006; Maki-Yonekura & Yonekura, 2008). Both these types of microscopy can contribute in other ways to the knowledge of structure, but in this article we concentrate on high-voltage phase-contrast electron microscopy of unstained macromolecules most often embedded in ice, because this is the method of widest impact in structural biology.

19.6.3.3. Required properties of the illuminating electron beam

The important properties of the image in terms of defocus, astigmatism, and the presence and effect of amplitude or phase contrast are discussed in Section 19.6.5. Microscopes with field emission guns (FEGs) produce the best-quality incident electron beams. This is because the electrons from a FEG are emitted from a very small volume at the tip, which is the apparent source size. Once these electrons have been collected by the condenser lens and used to produce the illuminating beam, that beam of electrons is then very parallel (divergence of $\sim 10^{-2}$ mrad) and therefore spa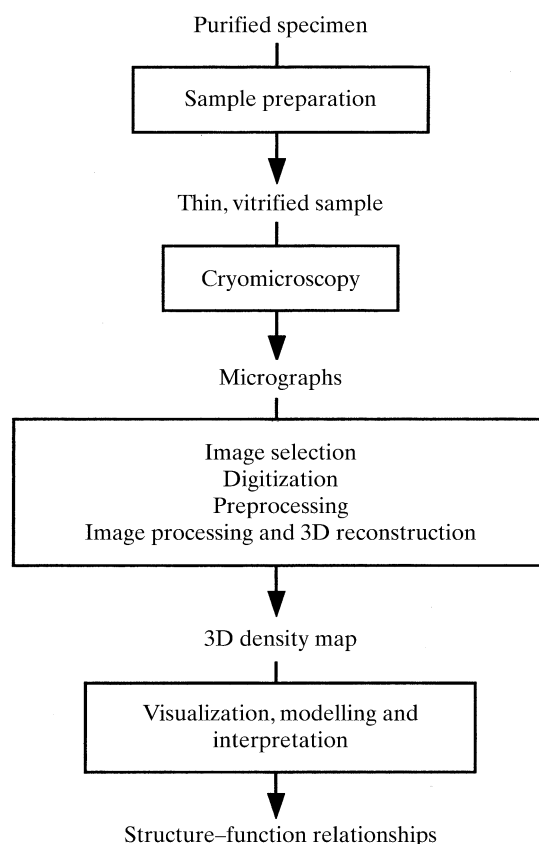tially coherent. Similarly, because the emitting tip of a FEG is not heated as much as a conventional thermionic tungsten source, the thermal-energy spread of the electrons is relatively small (0.5 to 1.0 eV) and the illuminating beam is closer to being monochromatic. Electron beams can also be produced by a normal heated tungsten source, which gives a less parallel beam with a larger energy spread, but is nevertheless adequate for cryoTEM if the highest resolution images are not required.

19.6.4. Three-dimensional electron cryomicroscopy of macromolecules

The determination of 3D structures by cryoTEM methods follows a common scheme for all macromolecules (Fig. 19.6.4.1). A more detailed discussion of the individual steps as applied to different classes of macromolecules appears in subsequent sections. Briefly, each specimen must be prepared in a relatively homo-geneous aqueous form (1D or 2D crystals or a suspension of single particles in a limited number of states) at relatively high concentration, rapidly frozen (vitrified) as a thin film, transferred into the electron microscope and imaged using low-dose selection and focusing procedures. The resulting images are more frequently being recorded using an electronic detector. Alternatively, if recorded on film, they must then be digitized. Digitized images are then processed using computer programs that allow different views of the specimen to be combined into a 3D reconstruction that can be interpreted in terms of other available structural, biochemical and molecular data.

19.6.4.1. Overview of conceptual steps

Radiation damage by the illuminating electron beam generally allows only one good picture (micrograph) to be obtained from

Purified specimen

Sample preparation

Thin, vitrified sample

Cryomicroscopy

Micrographs

Image selection
Digitization
Preprocessing
Image processing and 3D reconstruction

3D density map

Visualization, modelling and interpretation

Structure–function relationships

Figure 19.6.4.1
Flow diagram showing common procedures involved in cryoTEM from sample preparation to map interpretation.

595

each molecule or macromolecular assembly. In this micrograph, the signal-to-noise ratio of the 2D projection image is normally too small to determine the projected structure accurately. This
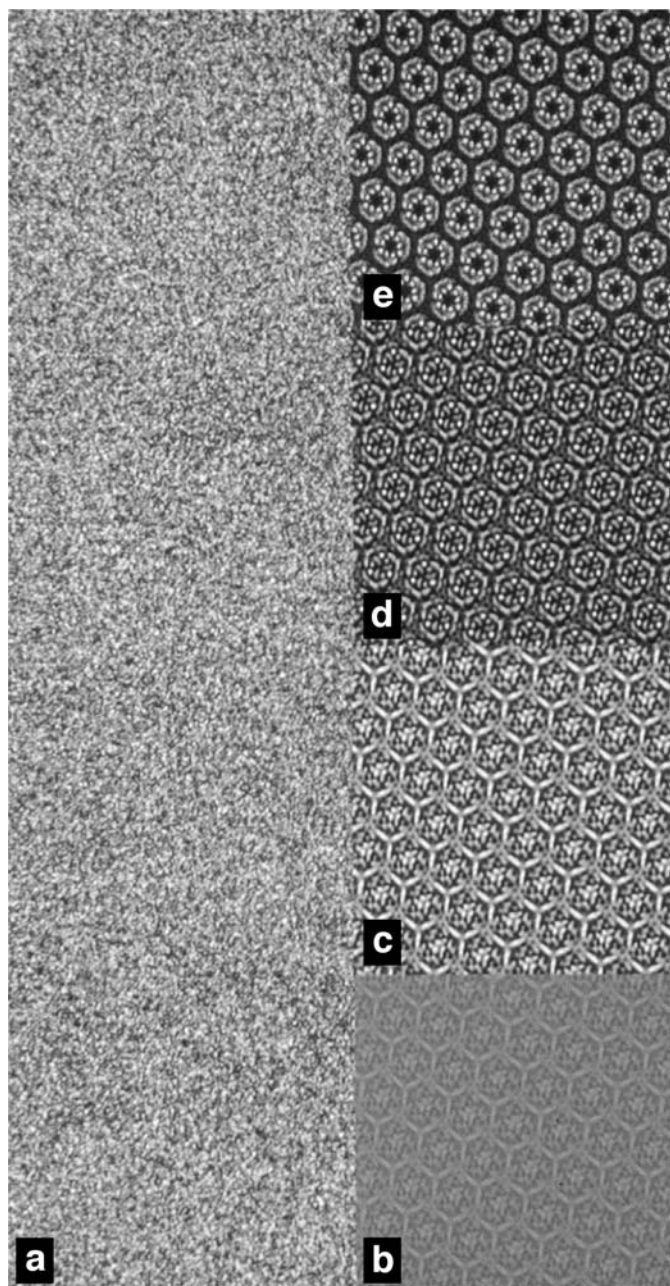
Figure 19.6.4.2
A display of the results at different stages of image processing of a digitized micrograph of a 2D crystal of bacteriorhodopsin. The left panel (*a*) shows an area of the raw digitized micrograph in which only electron noise is visible. The lower right panel (*b*) shows the results of the averaging of unit cells from the whole picture by unbending in real space and filtering in reciprocal space. The scale of the density in (*b*) is the same as that in the original micrograph, showing that the signal is very much weaker than the noise. Panel (*c*) shows the same density as in (*b*) but with contrast increased tenfold to show that the signal in the original picture is approximately $10\times$ below the noise level. Panel (*d*) shows the density after correction for the contrast-transfer function (CTF) due in this case to a defocus of 6000 Å. Panel (*e*) shows the density after further threefold crystallographic averaging (the space group is *p*3 with a cell dimension of 62.5 Å) and replacement of image amplitudes by electron-diffraction amplitudes. Panel (*e*) therefore shows an almost perfect atomic resolution image of the projected structure of bacteriorhodopsin. The trimeric rings of molecules are centred on the crystallographic threefold axes and the internal structure shows α-helical segments in the protein.

implies firstly that it is necessary to average many images of different molecules taken from essentially the same viewpoint to increase the signal-to-noise ratio, and secondly that many of these averaged projections, taken from different directions, must be combined to build up the information necessary to determine the 3D structure of the molecule. Thus, the two key concepts are: (1) averaging to a greater or lesser extent depending on resolution, particle size and symmetry to increase the signal-to-noise ratio; and (2) the combination of different projections to build a 3D map of the structure.

In addition, there are various technical corrections that must be made to the image data to allow an unbiased model of the structure to be obtained. These include correction for the phase contrast-transfer function (CTF) of the microscope and, at high resolution, for the effects of beam tilt. For crystals, it is also possible to combine electron-diffraction amplitudes with image phases to produce a more accurate structure (Unwin & Henderson, 1975), or to use new electron-diffraction data to improve a previous model (Gonen *et al.*, 2005), and in general to correct for loss of high-resolution contrast for any reason by 'sharpening' the data by application of a negative temperature factor (Havelka *et al.*, 1995; Rosenthal & Henderson, 2003; Fernandez *et al.*, 2008).

The idea of increasing the signal-to-noise ratio in electron images of unstained biological macromolecules by averaging was discussed in 1971 (Glaeser, 1971) and demonstrated in 1975 (Henderson & Unwin, 1975; Unwin & Henderson, 1975), though earlier work on stained specimens had shown the value of averaging to increase the signal-to-noise ratio (Klug & DeRosier, 1966). The improvement obtained, as in all repeated measurements, gives a factor of $N^{1/2}$ improvement in signal-to-noise ratio, where N is the number of times the measurement is made. The effect of averaging to produce an improvement in signal-to-noise ratio is seen most clearly in the processing of images from 2D crystals. For example, Fig. 19.6.4.2 shows the results of applying a sequence of corrections, beginning with averaging, to 2D crystals of bacteriorhodopsin in 2D space group *p*3. The panels show: (*a*) raw, digitized image, (*b*, *c*) 2D averaging, (*d*) correction for the microscope CTF, and (*e*) threefold crystallographic symmetry averaging of the phases and combination with electron-diffraction amplitudes. At each stage, the projected picture of the molecules gets clearer. The final stage results in a virtually noise-free projected structure for the molecule at near-atomic (3 Å) resolution.

The earliest successful application of the idea of combining projections to reconstruct the 3D structure of a biological assembly was made by DeRosier & Klug (1968). The idea is that each 2D projection corresponds after Fourier transformation to a central section of the 3D transform of the assembly. If enough independent projections are obtained, then the 3D transform will have been fully sampled and the structure can then be obtained by back-transformation of the averaged, interpolated and smoothed 3D transform. This procedure is shown schematically for a 3D object in the shape of a duck, which represents the molecule whose structure is being determined (Fig. 19.6.4.3).

In practice, the implementation of these concepts has been carried out in a variety of ways, since the experimental strategy and type of computer analysis used depends on the type of specimen, especially the molecular mass of the individual molecule, its symmetry and whether or not it assembles into an aggregate with 1D, 2D or 3D periodic order.
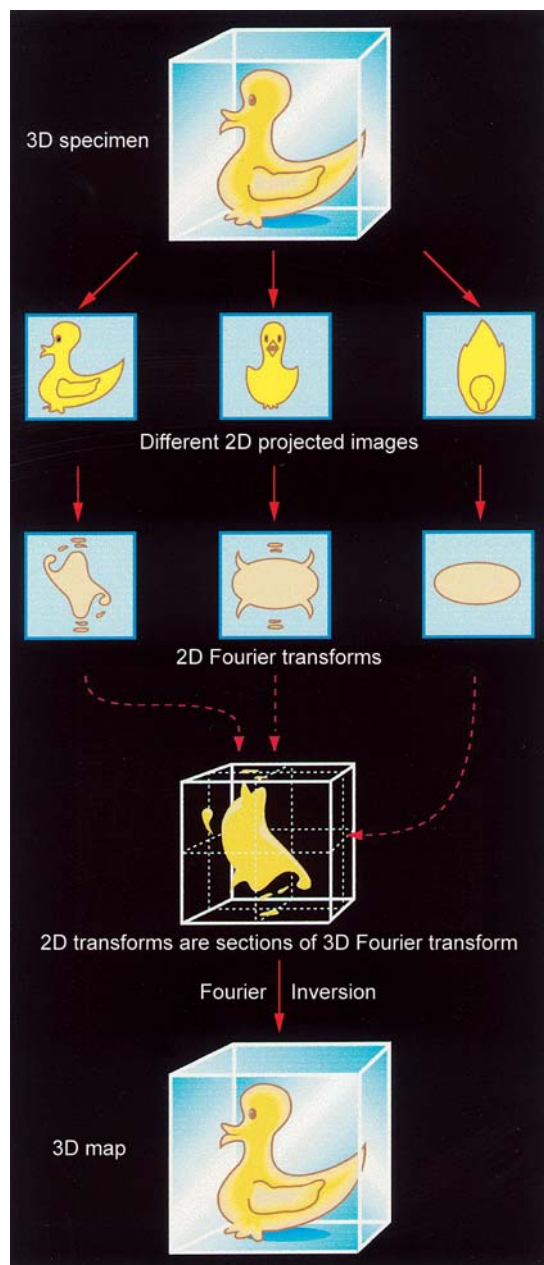
Figure 19.6.4.3
Schematic diagram to illustrate the principle of 3D reconstruction. Each 2D projected image, as recorded on the micrograph and after CTF correction, represents a section through the 3D Fourier transform. This is called the projection theorem. After accumulation of enough information from enough different views, a 3D map of the structure can be calculated by Fourier inversion.

19.6.4.2. Classification of macromolecules

The symmetry of a macromolecule or supramolecular complex is the primary determinant of how specimen preparation, microscopy and 3D image reconstruction are performed (Sections 19.6.4.3, 19.6.4.4 and 19.6.5). The classification of molecules according to their level of periodic order and symmetry (Table 19.6.4.1) provides a logical and convenient way to consider the means by which specimens are studied in 3D by microscopy.

Each type of specimen offers a unique set of challenges in obtaining 3D structural information at the highest possible resolution. The best resolutions achieved by 3D EM methods to date, at about 2–4 Å, have been obtained with several thin 2D crystals, in large part due to their excellent order, with helical

arrays and icosahedral single particles now crossing the 4 Å barrier (Cheng & Walz, 2009).

With the exception of true 3D crystals, which must be sectioned to make them thin enough to study by transmission electron microscopy, the resolution obtained with biological specimens is generally dictated by the preservation of periodic order, and the symmetry and complexity of the object. Hence, studies for example of 2D crystals of the aquaporin membrane channel (Gonen *et al.*, 2005), helical acetylcholine receptor tubes (Miyazawa *et al.*, 2003) and bacterial flagella (Yonekura, Maki-Yonekura & Namba, 2003), three icosahedral virus capsids (Yu, Jin & Zhou, 2008; Zhang *et al.*, 2008; Chen *et al.*, 2009), the 70S *E. coli* ribosome (LeBarron *et al.*, 2008), and HIV trimers obtained by sub-tomogram averaging (Liu, Bartesaghi *et al.*, 2008), have yielded 3D density maps at resolutions of 1.9, 4.0, 4.0, 4.0, 3.8, 3.8, 6.7 and 19 Å, respectively.

If high resolution were the sole objective of EM, it would be necessary, given the capabilities of existing technology, to try to form well ordered 2D crystals, helical assemblies or icosahedral particles of each macromolecule of interest. Indeed, a number of different crystallization techniques have been devised (*e.g.* Yoshimura *et al.*, 1990; Kornberg & Darst, 1991; Jap *et al.*, 1992; Kubalek *et al.*, 1994; Hasler *et al.*, 1998; Wilson-Kubalek *et al.*, 1998; Dang *et al.*, 2005; Schmidt-Krey, 2007) and some of these have yielded new structural information about otherwise recalcitrant molecules like RNA polymerase (Polyakov *et al.*, 1998). However, despite the obvious technological advantages of having a molecule present in a highly ordered form, most macromolecules function not as highly ordered crystals or helices but instead as single particles (*e.g.* many enzymes) or, more likely, in concert with other macromolecules as occurs in supramolecular assemblies. Also, crystallization tends to constrain the number of conformational states a molecule can adopt and the crystal conformation might not be functionally relevant. Hence, though resolution may be restricted to less than that realized in the bulk of current X-ray crystallographic studies, cryoTEM methods provide a powerful means to study molecules that resist crystallization in 1D, 2D or 3D. These methods allow one to explore the dynamic events, different conformational states (as induced, for example, by altering the microenvironment of the specimen) and macromolecular interactions that are the key to understanding how each macromolecule functions.

19.6.4.3. Specimen preparation

The goal in preparing specimens for cryoTEM is to keep the biological sample in its native state as closely as possible in order to preserve the structure to atomic or near-atomic resolution in the microscope and during microscopy. The methods by which numerous types of macromolecules and macromolecular complexes have been prepared for cryoTEM studies are now well established (Adrian *et al.*, 1984; Bellare *et al.*, 1988; Dubochet *et al.*, 1988; Grassucci *et al.*, 2007). Most such methods involve cooling samples at a rate fast enough to permit vitrification (to a solid glass-like state) rather than crystallization of the bulk water. Noncrystalline biological macromolecules are typically vitrified by applying a small (often <5 μl) aliquot of a purified ~0.2–5 mg ml^{-1} suspension of sample to an EM grid coated with a carbon or holey carbon support film. The grid, secured with a pair of forceps and suspended over a container of ethane or propane cryogen slush (maintained near its freezing point by a reservoir of liquid nitrogen), is blotted nearly dry with a piece of filter paper. The grid is then plunged into the cryogen, and the sample, if thin

Table 19.6.4.1
Classification of macromolecules according to periodic order and symmetry

Periodic order	Type	Symmetry	Example macromolecule/complex	Representative reference
0D	Point group	C_1	70S ribosome (bacterial)	Villa *et al.* (2009)
		C_1	80S ribosome (mammalian)	Chandramouli *et al.* (2008)
		C_1	Centriole	Kenney *et al.* (1997)
		C_1	ATP synthase (mitochondrial)	Rubinstein *et al.* (2003)
		C_1	ATP synthase (yeast)	Lau *et al.* (2008)
		C_1	Yeast RNA polymerase III	Fernandez-Tornero *et al.* (2007)
		C_1	P-ATPase (*E. coli*)	Heitkamp *et al.* (2009)
		C_1	V-ATPase (bovine brain)	Gregorini *et al.* (2007)
		C_1	V-ATPase (*Manduca sexta*)	Muench *et al.* (2009)
		C_1	Bacteriophage φ29 virion/ghost	Tang *et al.* (2008)
		C_2	Transferrin–transferrin-receptor complex	Cheng *et al.* (2004)
		C_2	Gp130–receptor complex	Matadeen *et al.* (2007)
		C_2	Voltage-gated calcium channel	Wang *et al.* (2004)
		C_3	Mg-chelatase ID complex	Elmlund *et al.* (2008)
		C_4	Ryanodine receptor channel	Ludtke *et al.* (2005)
		C_4	CLIC2–ryanodine-receptor complex	Meng *et al.* (2009)
		C_5	Bacteriophage φ29 head	Tao *et al.* (1998)
		C_5	Hemocyanin (*Nautilus pompilius*)	Gatsogiannis *et al.* (2007)
		C_6	Plant plasma membrane H^+-ATPase	Ottmann *et al.* (2007)
		C_7	GroEL–GroES complexes	Ranson *et al.* (2006)
		C_7	Cytolysin (*Vibrio cholerae*)	He & Olson (2010)
		C_8	Outer membrane protein Wza (*E. coli*)	Ford *et al.* (2009)
		C_{12}	Bacteriophage T7 connector	Agirrezabala *et al.* (2005)
		C_{17}	TMV disc	Bloomer *et al.* (1978)
		C_{20}	Type III secretion injectisome	Marlovits *et al.* (2006)
		D_2	Phosphorylase kinase holoenzyme	Venien-Bryan *et al.* (2009)
		D_5	Hemocyanin (*Rapana thomasiana*)	Cheng *et al.* (2006)
		D_6	Clathrin coats	Fotin *et al.* (2004)
		D_6	Haemoglobin (*Lumbricus terrestris*)	Schatz *et al.* (1995)
		D_7	GroEL	Ludtke *et al.* (2008)
		D_7	20S proteosome	Rabl *et al.* (2008)
		D_8	Double aptosome	Yu *et al.* (2006)
		D_{48}	Recombinant ribonucleoprotein vault	Mikyas *et al.* (2004)
		T	Dps protein	Grant *et al.* (1998)
		O	Pyruvate dehydrogenase core	Mattevi *et al.* (1992)
		I	COPII coat assembly	Stagg *et al.* (2008)
		I	Human PDC E2 and tE2 cores	Yu, Hiromasa *et al.* (2008)
		I	Tricorn protease	Walz *et al.* (1997)
		I	Icosahedral viruses	Baker *et al.* (1999)
1D	Screw axis (helical)†		F-actin–fimbrin/plastin ABD2 complex	Galkin *et al.* (2008)
			Acto-myosin filament	Milligan (1996)
			Acetylcholine receptor tubes	Miyazawa *et al.* (2003)
			Bacterial flagella	Yonekura, Maki-Yonekura & Namba (2003)
			Bacterial ParM filament	Orlova *et al.* (2007)
			Bacterial type IV pilus	Craig *et al.* (2006)
			Bacteriophage fd	Wang *et al.* (2006)
			F-BAR membrane tubule	Frost *et al.* (2008)
			Microtubule	Li *et al.* (2002)
			P-type ATPases	Pomfret *et al.* (2007)
			Tobacco mosaic virus	Sachse *et al.* (2007)
2D	2D space group (2D crystal)	$p12_1$	Tubulin sheet	Nogales *et al.* (1998)
		$p22_12_1$	Prostaglandin E synthase	Jegerschold *et al.* (2008)
		$p22_12_1$; $p6$	Microsomal glutathione transferase 1	Holm *et al.* (2006)
		$p3$	Bacteriorhodopsin membrane	Henderson *et al.* (1990)
		$p321$	Light-harvesting complex II	Kühlbrandt *et al.* (1994)
		$p42_12$	Aquaporin AQPO membrane	Gonen *et al.* (2005)
		$p6$	Gap junction membrane	Fleishman *et al.* (2004)
3D	3D space group (3D crystal)	$P2_12_12_1$	Myosin S1 protein crystal	Winkelmann *et al.* (1991)
		$P6_5$ or $P6_4$	Insect flight muscle	Liu *et al.* (2006)

† The symmetry of a helical structure is defined by an n_m screw axis, which combines a rotation of $2\pi/n$ radians about an axis followed by a translation of m/n of the repeat distance. Because many helical structures are polymorphic, a different n_m symmetry is needed to specify each polymorph. This designation can be confusing: for example, for tobacco mosaic virus $n_m = 16.333_{0.333}$, because the helical translational repeat consists of 49 subunits in three turns of the basic helix.

enough ($\sim$0.2 μm or less), is vitrified in millisecond or shorter time periods (Mayer & Astl, 1992; Berriman & Unwin, 1994; White *et al.*, 1998; Kasas *et al.*, 2003).

The ability to freeze samples on a timescale of milliseconds affords cryoTEM one of its unique and perhaps still under-utilized advantages: capturing and visualizing dynamic structural events that occur over time periods of a few milliseconds or longer. Several devices that allow samples to be perturbed in a variety of ways as they are plunged into a cryogen have been described (*e.g.* Subramaniam *et al.*, 1993; Berriman & Unwin, 1994; Siegel *et al.*, 1994; Trachtenberg, 1998; White *et al.*, 1998, 2003; Shaikh *et al.*, 2009), and there are now commercially

available freeze-plungers (*e.g.* Iancu *et al.*, 2006; Melanson, 2009). Examples of the use of such devices include spraying acetylcholine onto its receptor to cause the receptor channel to open (Unwin, 1995), lowering the pH of an enveloped virus sample to initiate early events of viral fusion (Fuller *et al.*, 1995), inducing a temperature jump with a flash-tube system to study phase transitions in liposomes (Siegel & Epand, 1997), or mixing myosin S1 fragments with F-actin to examine the geometry of the cross-bridge powerstroke in muscle (Walker *et al.*, 1999).

Crystalline (2D) samples can fortunately often be prepared for cryoTEM by means of simpler procedures, and vitrification of the bulk water is not always essential to achieve success (Cyrklaff & Kühlbrandt, 1994). Such specimens may be applied to the carbon film on an EM grid by normal adhesion methods, washed with 1–2% solutions of solutes like glucose, trehalose or tannic acid, blotted gently with filter paper to remove excess solution, air dried, loaded into a cold holder, inserted into the microscope, and, finally, cooled to liquid-nitrogen temperature.

19.6.4.4. Microscopy

Once the vitrified specimen is inserted into the microscope and sufficient time is allowed ($\sim$15 min) for the specimen stage to stabilize to minimize drift and vibration, microscopy is performed to generate a set of images that, with suitable processing procedures, can later be used to produce a reliable 3D reconstruction of the specimen at the highest possible resolution. To achieve this goal, imaging must be performed at an electron dose that minimizes beam-induced radiation damage to the specimen, with the objective lens of the microscope defocused to enhance phase contrast from the weakly scattering, unstained biological specimen, and under conditions that keep the specimen below the devitrification temperature ($\sim$$-140\,°C$) and minimize its contamination.

The microscopist locates specimen areas suitable for image recording by searching the EM grid at very low magnification ($\leq$3000$\times$) to keep the irradiation level quite low (<0.05 e $\text{Å}^{-2}\,\text{s}^{-1}$) while assessing sample quality. In microscopes operated at 200 keV or higher, where image contrast is very weak, it is helpful to perform the search procedure with the assistance of a CCD camera or a video-rate TV-intensified camera system. Indeed, these are now much more sensitive than looking at a phosphor screen by eye. For some specimens, like thin 2D crystals, searching is conveniently performed while viewing the low-magnification high-contrast image produced by using the diffraction lens to give a slightly defocused electron-diffraction pattern. Electronic detectors also have automatic histogram expansion settings that allow amplification of small contrast differences on a display monitor. These become more-or-less essential when using high-voltage (300 keV) microscopes.

After a desired specimen area is identified, the microscope is switched to high-magnification mode for focusing and astigmatism correction. These adjustments are typically performed in a region $\sim$2–5 μm away from the chosen area at the same or higher magnification than that used for final image recording. The choice of magnification, defocus level, accelerating voltage, beam coherence, electron dose and other operating conditions is dictated by several factors. The most significant ones are the size of the particle or crystal unit cell being studied, the anticipated resolution of the images and the requirements of the image processing needed to compute a 3D reconstruction to the desired resolution. For most specimens at required resolutions from 3 to 30 Å, images are typically recorded at 25 000–50 000$\times$ magnification with an electron dose of between 5 and 20 e Å^{-2}. These conditions yield micrographs of sufficient optical density (film OD 0.2–1.5) or dynamic range (CCD detector) and image resolution for subsequent image-processing steps (Section 19.6.5). All modern EMs provide some mode of low-dose operation for imaging beam-sensitive, vitrified biological specimens.

The intrinsic low contrast of unstained specimens makes it impossible to observe and focus on specimen details directly as is routine with stained or metal-shadowed specimens. Focusing, aimed to enhance phase contrast in the recorded images while minimizing beam damage to the desired area, is achieved by judicious defocusing on a region that is adjacent to the region to be photographed and preferably situated on the microscope tilt axis. The appropriate focus level is set by adjusting the appearance of either the Fresnel fringes that occur at the edges of holes in the carbon film or the 'phase granularity' from the carbon support film.

Unfortunately, electron images do not give a direct rendering of the specimen density distribution. The relationship between image and specimen is described by the CTF which is characteristic of the particular microscope used, the specimen and the conditions of imaging. The microscope CTF arises from the objective-lens focal setting and from the spherical aberration present in all electromagnetic lenses, and varies with the defocus and accelerating voltage according to equation (19.6.4.1), an expression that includes both phase and amplitude contrast components. First, however, it is useful to consider briefly the essentials of amplitude contrast and phase contrast, two concepts carried over from optical microscopy. Amplitude contrast refers to the nature of the contrast in an image of an object that absorbs the incident illumination or scatters it in any other way so that a portion of it is lost. As a result, the image appears darker where greater absorption occurs. Phase contrast is required if an object is transparent (*i.e.* it is a pure phase object) and does not absorb but only scatters the incident illumination. Biological specimens for cryoTEM are almost pure phase objects and the scattering is relatively weak. Hence, the simple theory of image formation by a weak phase object applies (Reimer & Kohl, 2008; Spence, 2009). An exactly in-focus image of a phase object has no contrast variation since all the scattered illumination is focused back to equivalent points in the image of the object from which it was scattered. In optical microscopy, the use of a quarter wave plate can retard the phase of the direct unscattered beam, so that an in-focus image of a phase object has very high 'Zernicke' phase contrast (Glaeser, 2008*a*). However, there is as yet no simple quarter wave plate for electrons, so instead phase contrast is created by introducing phase shifts into the diffracted beams by adjustment of the excitation of the objective lens so that the image is slightly defocused. In addition, since all matter is composed of atoms and the electric potential inside each atom is very high near the nucleus, even the electron-scattering behaviour of the light atoms found in biological molecules deviates from that of a weak phase object. For a more in-depth discussion of this the reader should refer to Reimer & Kohl (2008) or Spence (2009). In practice, the proportion of 'amplitude' contrast is about 7% at 100 kV, 5% at 200 kV and 4% at 300 kV for low-dose images of protein molecules embedded in ice.

The overall dependence of the CTF on resolution, wavelength, defocus and spherical aberration is

$$\text{CTF}(\nu) = -\left\{\left(1 - F_{\text{amp}}^2\right)^{1/2}\sin[\chi(\nu)] + F_{\text{amp}}\cos[\chi(\nu)]\right\},$$

$$(19.6.4.1)$$

where $\chi(\nu) = \pi\lambda\nu^2(\Delta f - 0.5C_s\lambda^2\nu^2)$, ν is the spatial frequency (in $\mathring{A}^{-1}$), F_{amp} is the fraction of amplitude contrast, λ is the electron wavelength (in $\mathring{A}$), where $\lambda = 12.3/(V + 0.000000978V^2)^{1/2}$ (= 0.037, 0.025 and 0.020 $\mathring{A}$ for 100, 200 and 300 keV electrons, respectively), V is the voltage (in volts), Δf is the underfocus (in $\mathring{A}$) and C_s is the spherical aberration of the objective lens of the microscope (in $\mathring{A}$).

In addition, the CTF is attenuated by an envelope or damping function that depends upon the spatial and temporal coherence of the beam, specimen drift and other factors (Erickson & Klug, 1971; Wade & Frank, 1977; Wade, 1992). Representative CTFs for different amounts of defocus on a conventional tungsten and a FEG microscope are illustrated in Fig. 19.6.4.4. For a particular defocus setting of the objective lens, phase contrast in the electron image is positive and maximal only at a few specific spatial frequencies. Contrast is either lower than maximal, completely absent or it is opposite (inverted or reversed) from that at other frequencies. Hence, as the objective lens is focused, the electron microscopist selectively accentuates image details of a particular size.

Images are typically recorded 0.8–3.0 μm underfocus to enhance specimen features in the 20–40 $\mathring{A}$ size range and thereby facilitate phase-origin and specimen-orientation search procedures carried out in the image-processing steps (Section 19.6.5). However, this level of underfocus also enhances contrast in lower-resolution maps, which may help in interpretation. To obtain results at sub-nanometre (<10 $\mathring{A}$) resolution, it is normal to record, process and combine data from several micrographs that span a range of defocus levels (*e.g.* Unwin & Henderson, 1975; Böttcher *et al.*, 1997). This strategy assures good information transfer at all spatial frequencies up to the limiting resolution but requires careful compensation for the effects of the microscope CTF during image processing. Also, the recording of image focal pairs or focal series from a given specimen area can be beneficial in determining origin and orientation parameters for processing of images of single particles (*e.g.* Cheng *et al.*, 1992; Conway & Steven, 1999).

Most high-resolution cryoTEM studies are now performed with microscopes operated at 200 keV or higher and with FEG electron sources (*e.g.* Zemlin, 1992; Zhou & Chiu, 1993; Ludtke *et al.*, 2008; Yu, Jin & Zhou, 2008; Zhang *et al.*, 2008). The high coherence of a FEG source ensures that phase contrast in the images remains strong out to high spatial frequencies (>1/3.5 $\mathring{A}^{-1}$) even for highly defocused images. The use of higher voltages provides potentially higher resolution (greater depth of field – *i.e.* less curvature of the Ewald sphere – owing to the smaller electron-beam wavelength), better beam penetration (less multiple scattering), reduced problems with specimen charging that plague microscopy of unstained or uncoated vitrified specimens (Brink *et al.*, 1998) and reduced phase shifts associated with beam tilt.

Images are recorded on photographic film or on an electronic camera with either flood-beam or spot-scan procedures. Film, with its advantages of low cost, large field of view and high resolution (~10 μm), has remained the primary image-recording medium for most high-resolution cryoTEM applications, despite disadvantages of high background fog and need for chemical development and digitization. Electronic (usually phosphor/fibre optic/CCD) cameras provide image data directly in digital form and with very low background noise, but suffer from higher cost, limited field of view, limited spatial resolution caused by poor point-spread characteristics and a fixed pixel size (typically between 14 and 24 μm). They are useful, for example, for precise
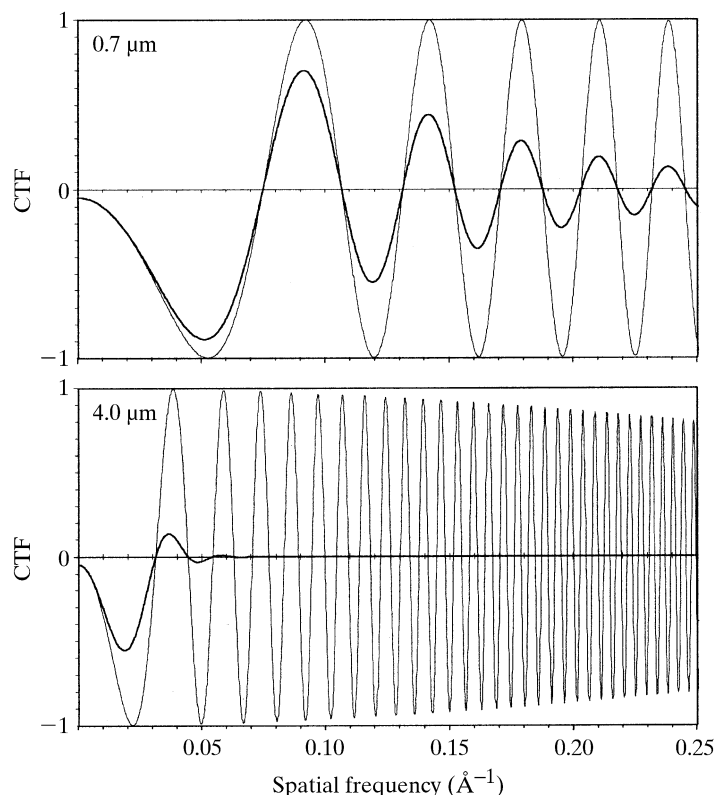
Figure 19.6.4.4
Representative plots of the microscope CTF as a function of spatial frequency, for two different defocus settings (0.7 and 4.0 μm underfocus) and for a field-emission (light curve) or tungsten (dark curve) electron source. All plots correspond to electron images formed in an electron microscope operated at 200 kV with objective-lens aberration coefficients $C_s = C_c = 2.0$ mm and assuming amplitude contrast of 4.8% (Toyoshima *et al.*, 1993). The spatial coherence, which is related to the electron source size and expressed as β, the half-angle of illumination, for tungsten and FEG electron sources was fixed at 0.3 and 0.015 mrad, respectively. Likewise, the temporal coherence (expressed as ΔE, the energy spread) was fixed at 1.6 and 0.5 eV for tungsten and FEG sources. The combined effects of the poorer spatial and temporal coherence of the tungsten source leads to a significant dampening, and hence loss of contrast, of the CTF at progressively higher resolutions compared with that observed in FEG-equipped microscopes. The greater number of contrast reversals with higher defocus arises because of the greater out-of-focus phase shifts.

focusing and adjustment of astigmatism (*e.g.* Krivanek & Mooney, 1993; Sherman *et al.*, 1996) and are increasingly used to acquire image data for 3D reconstruction studies (*e.g.* Booth *et al.*, 2004; Sander *et al.*, 2005; Booth *et al.*, 2006; Chen *et al.*, 2008). There is a useful comparison of the MTF and DQE at different spatial frequencies between film and several electronic detectors (McMullan, Chen *et al.*, 2009). In summary, at present, all image recording is better at low (*e.g.* 120 kV) voltage with little to choose between different recording media, but film, in 2009, is still best at 300 keV.

For studies in which specimens must be tilted to collect 3D data, such as with 2D crystals, single particles that adopt preferred orientations on the EM grid or specimens requiring tomography, microscopy is performed in essentially the same way as described above. However, the limited tilt range (±60–70°) of most microscope goniometers can lead to non-isotropic resolution in the 3D reconstructions (the 'missing wedge' or 'missing cone' problem), and tilting generates a constantly varying defocus across the field of view in a direction normal to the tilt axis. The effects caused by this varying defocus level must be corrected in high-resolution applications (Henderson *et al.*, 1990).

19.6.4.5. Selection and preprocessing of digitized images

Before any image analysis or classification of the molecular images can be done, a certain amount of preliminary checking and normalization is required to ensure there is a reasonable chance that a homogeneous population of molecular images has been obtained. First, good-quality micrographs are selected in which the electron exposure is correct, there is negligible image drift or blurring, and there is minimal astigmatism and a reasonable amount of defocus to produce good phase contrast. This is usually done by visual examination and optical diffraction or examination of the computed diffraction pattern.

Once the best micrographs have been chosen, if they are on film they must be scanned and digitized on a suitable densitometer. The sizes of the steps between digitization of optical density, and the size of the sample aperture over which the optical density is averaged by the densitometer, must be sufficiently small to sample the detail present in the image at fine enough intervals (DeRosier & Moore, 1970). Normally, a circular (or square) sample aperture of diameter (or length of side) equal to the step between digitization is used. This avoids digitizing overlapping points, without missing any of the information recorded in the image. The size of the sample aperture and digitization step depends on the magnification selected and the resolution required. A value of one-quarter to one-third of the required limit of resolution (measured in µm on the emulsion) is normally ideal, since it avoids having too many data points (and therefore wasting computer resources) without losing anything during the measurement procedure. For a $40\,000\times$ image, on which a resolution of 10 Å at the specimen is required, a step size of 10 µm $[= (1/4)(10\,\text{Å} \times 40\,000/10\,000\,\text{Å}\,\mu\text{m}^{-1})]$ would be suitable.

The best area of an image of a helical or 2D crystal specimen can then be boxed off using a soft-edged mask. For images of single particles, a small, often circular region surrounding each particle is selected to create a stack of many individual particles. In the later steps of image processing, because the orientation and position of each particle are refined by comparing the amplitudes and phases of their Fourier components, it is important to remove spurious features around the edge of each particle and to make sure the different particle images are on the same scale. This is normally done by masking off a circular area centred on each particle and floating the density so that the average around the perimeter becomes zero (DeRosier & Moore, 1970). The edge of the mask is apodized by applying a soft cosine bell shape to the original densities so they taper towards the background level. Finally, to compensate for variations in the exposure due to ice thickness or electron dose, most people normalize the stack of individual particle images so that the mean density and mean density variation over the field of view are set to the same values for all particles (Carrascosa & Steven, 1978).

Once some good particles or crystalline areas for 1D or 2D crystals have been selected, digitized and masked and their intensity values have been normalized, true image processing can begin.

19.6.5. Image processing and 3D reconstruction

Although the general concepts of signal averaging, together with combining different views to reconstruct the 3D structure, are common to the different computer-based procedures that have been implemented, it is important to emphasize one or two preliminary points. First, a homogeneous set of particles must be selected for inclusion in the 3D reconstruction. This selection may be made by eye to eliminate obviously damaged particles or impurities, or by the use of multivariate statistical analysis (van Heel & Frank, 1981) or some other classification scheme, such as local cross-correlation (Roseman, 2003). This allows a subset of the particle images to be used to determine the structure of a better-defined entity. All image-processing procedures require the determination of the same parameters that are needed to specify unambiguously how to combine the information from each micrograph or particle. These parameters are: the magnification, defocus, astigmatism and, at high resolution, the beam tilt for each micrograph; the electron wavelength used (*i.e.* accelerating voltage of the microscope); the spherical aberration coefficient, C_s, of the objective lens; and the orientation and phase origin for each particle or unit cell of the 1D, 2D or 3D crystal. There are 13 parameters for each particle, eight of which may be common to each micrograph and two or three (C_s, accelerating voltage, magnification) to each microscope. The different general approaches that have been used in practice to determine the 3D structure of different classes of macromolecular assemblies from one or more electron micrographs are listed in Table 19.6.5.1.

The precise way in which each general approach codes and determines the particle or unit-cell parameters varies greatly and is not described in detail. Much of the computer software used in image-reconstruction studies is relatively specialized compared with that used in the more mature field of macromolecular X-ray crystallography. In part, this may be attributed to the large diversity of specimen types amenable to cryoTEM and reconstruction methods. As a consequence, image-reconstruction software is still evolving quite rapidly, and references to software packages cited in Table 19.6.5.1 are likely to become quickly outdated. Extensive discussion of algorithms and software packages may be found in several special issues of *Journal of Structural Biology* [Vol. 116, pp. 1–249 (1996); Vol. 120, pp. 207–396 (1997); Vol. 125, pp. 95–254 (1999); Vol. 133, pp. 89–266 (2001); Vol. 138, pp. 1–155 (2002); Vol. 144, pp. 1–252 (2003); Vol. 145, pp. 1–180 (2004); Vol. 157, pp. 1–296 (2007); Vol. 160, pp. 263-404 (2007); and Vol. 161, pp. 219–480 (2008)]. Tomography is the topic of Volumes 120, 138 and 161, single-particle cryoTEM is covered in Volume 133, particle-picking algorithms are covered in Volume 145 and electron crystallography of membrane proteins is covered in Volume 160.

In practice, attempts to determine or refine some parameters may be affected by the inability to determine accurately one of the other parameters. The solution of the structure is therefore an iterative procedure in which reliable knowledge of the parameters that describe each image is gradually built up to produce a more and more accurate structure until no more information can be squeezed out of the micrographs. At this point, if any of the origins or orientations are wrongly assigned, there will be a loss of detail and a decrease in signal-to-noise ratio in the map. If a better-determined or higher-resolution structure is required, it would then be necessary to record images on a better microscope or to prepare new specimens and record better pictures.

The reliability and resolution of the final reconstruction can be measured using a variety of indices. For example, the DPR (Frank *et al.*, 1981), the FSC (van Heel, 1987*b*) and the Q factor (van Heel & Hollenberg, 1980) are three such measures. The DPR is the mean phase difference, as a function of resolution, between the structure factors from two independent reconstructions, often calculated by splitting the image data into two halves. The FSC is a similar calculation of the mean correlation

Table 19.6.5.1
Methods of three-dimensional image reconstruction

Structure type (symmetry)	Method	Reference(s) to technical/theoretical details
Asymmetric (point group C_1)	Random conical tilt (software packages)	Radermacher *et al.* (1987); Radermacher (1988) Frank *et al.* (1996); Baxter *et al.* (2007); Shaikh *et al.* (2008)
	Angular reconstitution (software package)	van Heel (1987*a*); Schatz *et al.* (1995) van Heel *et al.* (1996)
	Weighted back-projection	Radermacher (1991, 1992)
	Radon transform alignment	Radermacher (1994); Ludtke *et al.* (1999); Tang *et al.* (2007)
	Reference-based alignment	Penczek *et al.* (1994)
	Reference-free alignment	Schatz & van Heel (1990); Penczek *et al.* (1992)
	Simulated-annealing alignment	Ogura & Sato (2006)
	Cross-correlation of common lines	Hall *et al.* (2007)
	Ab initio maximum likelihood	Prust *et al.* (2009)
	Maximum-likelihood multi-reference refinement	Scheres *et al.* (2005)
	Fourier reconstruction and alignment	Grigorieff (1998, 2007)
	Orthogonal tilt reconstruction	Leschziner & Nogales (2006)
	Tomographic tilt series and remote control of microscope†	Olins *et al.* (1983); Fung *et al.* (1996); Ziese *et al.* (2002, 2003); Zheng *et al.* (2004); Mastronarde (2005); Nickell *et al.* (2005); Zheng *et al.* (2007)
Symmetric (point groups C_n, D_n; $n > 1$)	Angular reconstitution (software package)	van Heel (1987*a*); Schatz *et al.* (1995) van Heel *et al.* (1996)
	Fourier–Bessel synthesis	Tao *et al.* (1998)
	Reference-based alignment and weighted back-projection	Beuron *et al.* (1998); Ludtke *et al.* (1999); Grigorieff (2007); Tang *et al.* (2007)
Icosahedral (point group I)	Fourier–Bessel synthesis (common lines)	Crowther (1971); Fuller *et al.* (1996); Mancini *et al.* (1997); Thuman-Commike & Chiu (1997)
	Reference-based alignment	Crowther *et al.* (1994); Baker & Cheng (1996); Castón *et al.* (1999); Grigorieff (2007); Yan, Dryden *et al.* (2007)
	(software packages)	Crowther *et al.* (1996); Lawton & Prasad (1996); Zhou *et al.* (1998); Jiang, Li *et al.* (2001); Liang *et al.* (2002); Yan, Sinkovits & Baker (2007)
	Angular reconsitution	van Heel (1987*a*); Stewart *et al.* (1997)
	Model-free reconstruction	Cantele *et al.* (2003); Navaza (2003)
	Multi-path simulated annealing	Liu *et al.* (2007)
	Symmetry-adapted spherical harmonics	Liu, Cheng *et al.* (2008)
	Tomographic tilt series	Walz *et al.* (1997)
Helical	Fourier–Bessel synthesis	DeRosier & Klug (1968); DeRosier & Moore (1970); Stewart (1988); Toyoshima & Unwin (1990); Morgan & DeRosier (1992); Unwin (1993); Beroukhim & Unwin (1997); Miyazawa *et al.* (1999); Wang & Nogales (2005)
	(software packages and filament straightening routines)	Egelman (1986); Whittaker *et al.* (1995); Carragher *et al.* (1996); Crowther *et al.* (1996); Owen *et al.* (1996); Beroukhim & Unwin (1997); Yonekura, Toyoshima *et al.* (2003); Metlagel *et al.* (2007)
	Iterative helical real-space reconstruction	Egelman (2000, 2007*a*); Ramey *et al.* (2009)
2D crystal	Random azimuthal tilt	Henderson & Unwin (1975); Amos *et al.* (1982); Henderson *et al.* (1986); Baldwin *et al.* (1988); Henderson *et al.* (1990)
	(software packages)	Crowther *et al.* (1996); Hardt *et al.* (1996); Gipson, Zeng & Stahlberg (2007); Gipson, Zeng, Zhang & Stahlberg (2007)
	Single-particle refinement	Koeck *et al.* (2007)
3D crystal	Oblique section reconstruction	Crowther & Luther (1984); Winkler & Taylor (1994); Taylor *et al.* (1997)
	(software package)	Winkler & Taylor (1996)
	Sectioned 3D crystal	Winkelmann *et al.* (1991)

† Electron tomography is the subject of several recent reviews (Jonic *et al.*, 2008; McEwen *et al.*, 2008; Morris & Jensen, 2008; Steven & Baumeister, 2008; Bárcena & Koster, 2009; Bartesaghi & Subramaniam, 2009; Hoenger & McIntosh, 2009; Leis *et al.*, 2009; Li & Jensen, 2009), three special issues of *Journal of Structural Biology* [Vol. 120, pp. 207–395 (1997); Vol. 138, pp. 1–155 (2002); and Vol. 161, pp. 219–480 (2008)] and a book edited by Frank (2006*a*).

coefficient between the complex structure factors of the two halves of the data as a function of resolution. The *Q* factor is the mean ratio of the vector sum of the individual structure factors from each image divided by the sum of their moduli, again calculated as a function of resolution. Perfectly accurate measurements would have values of the DPR, FSC and *Q* factor of 0°, 1.0 and 1.0, respectively, whereas random data containing no information would have values of 90°, 0.0 and 0.0. The spectral signal-to-noise ratio (SSNR) criterion has been advocated as the best of all (Unser *et al.*, 1989): it effectively measures, as a function of resolution, the overall signal-to-noise ratio (squared) of the whole of the image data. It is calculated by taking into consideration how well all the contributing image data agree internally.

An example of a strategy for determination of the 3D structure of a new and unknown molecule without any symmetry and which does not crystallize might be as follows:

(1) Record a single-axis tilt series of particles embedded in negative stain, with a tilt range from −60° to +60°.

(2) Calculate 3D structures for each of several different particles using an *R*-weighted back-projection algorithm (Radermacher, 1992).

(3) Average 3D data for several particles in real or reciprocal space to get a reasonably good 3D model of the stain-excluding region of the particle.

(4) Record a number of micrographs of the particles embedded in vitreous ice.

(5) Use the 3D negative-stain model obtained in (3) with inverted contrast to determine the rough alignment parameters of the particle in the ice images.

(6) Calculate a preliminary 3D model of the average ice-embedded structure.

(7) Use the preliminary 3D model to determine more accurate alignment parameters for the particles in the ice images.

(8) Calculate a better 3D model.

(9) Determine defocus and astigmatism for each micrograph to allow CTF calculation and correct 3D model so that it represents the structure at high resolution.

(10) Keep adding images at different defocus levels to get an accurate structure at as high a resolution as possible.

(11) Correct the final structure for resolution-dependent contrast loss and apply a damping factor dependent on signal-to-noise ratio (Rosenthal & Henderson, 2003).

For large single particles with no symmetry, particles with higher symmetry or crystalline arrays, it should be possible to omit the negative-staining steps (1)–(3) and go straight to alignment of particle images from ice embedding, because the particle or crystal tilt angles can be determined internally from comparison of phases along common lines in reciprocal space or from the lattice or helix parameters from a 2D or 1D crystal.

The following discussion briefly outlines for a few specific classes of macromolecule the general strategy for carrying out image processing and 3D reconstruction.

19.6.5.1. 2D crystals

For 2D crystals, the general 3D reconstruction approach consists of the following steps. First, a series of micrographs of single 2D crystals are recorded at different tilt angles, with random azimuthal orientations. Each crystal is then unbent using cross-correlation techniques to identify the precise position of each unit cell (Henderson *et al.*, 1986), and amplitudes and phases of the Fourier components of the average of that particular view of the structure are obtained for the transform of the unbent crystal. The reference image used in the cross-correlation calculation can either be a part of the whole image masked off after a preliminary round of averaging by reciprocal-space filtering of the regions surrounding the diffraction spots in the transform, or it can be a reference image calculated from a previously determined 3D model. The amplitudes and phases from each image are then corrected for the CTF and beam tilt (Henderson *et al.*, 1986, 1990; Kunji *et al.*, 2000) and merged with data from many other crystals by scaling and origin refinement, taking into account the proper symmetry of the 2D space group of the crystal (Landsberg & Hankamer, 2007). Finally, the whole data set is fitted by least squares to constrained amplitudes and phases

along the lattice lines (Agard, 1983) prior to calculating a 3D map of the structure. The initial determination of the 2D space group can be carried out by a statistical test of the phase relationships in one or two images of untilted specimens (Valpuesta *et al.*, 1994). The absolute hand of the structure is automatically correct since the 3D structure is calculated from images whose tilt axes and tilt angles are known. Nevertheless, care must be taken not to make any of a number of trivial mistakes that would invert the hand. Recent efforts have been devoted to create a user-friendly interface for image processing of 2D crystals (Gipson, Zeng & Stahlberg, 2007; Gipson, Zeng, Zhang & Stahlberg, 2007; Zeng *et al.*, 2007). The entire topic of processing images of 2D crystals and evaluating the data has been the subject of several publications and reviews (*e.g.* Yeager *et al.*, 1999; Unger, 2000; Renault *et al.*, 2006; Hite *et al.*, 2007; Kovacs *et al.*, 2008).

19.6.5.2. Helical particles

The basic steps involved in processing and 3D reconstruction of helical specimens include the following. First, record a series of micrographs of vitrified particles suspended over holes in a perforated carbon support film. The micrographs are digitized and Fourier transformed to determine image quality (astigmatism, drift, defocus, presence and quality of layer lines, *etc.*). Individual particle images are boxed, floated and apodized within a rectangular mask. The parameters of helical symmetry (number of subunits per turn and pitch) must be determined by indexing the computed diffraction patterns. If necessary, simple spline-fitting procedures may be employed to 'straighten' images of curved particles (Egelman, 1986), and the image data may be reinterpolated (Owen *et al.*, 1996) to provide more precise sampling of the layer-line data in the computed transform. Once a preliminary 3D structure is available, a much more sophisticated refinement of all the helical parameters can be used to unbend the helices onto a predetermined average helix so that the contributions of all parts of the image are correctly treated (Beroukhim & Unwin, 1997). The layer-line data are extracted from each particle transform and two phase-origin corrections are made: one to shift the phase origin to the helix axis (at the centre of the particle image) and the other to correct for effects caused by having the helix axis tilted out of the plane normal to the electron beam in the electron microscope. The layer-line data are separated out into near- and far-side data, corresponding to contributions from the near and far sides of each particle imaged. The relative rotations and translations needed to align the different transforms are determined so the data may be merged and a 3D reconstruction computed by Fourier–Bessel inversion procedures (DeRosier & Moore, 1970). Determination of the absolute hand requires comparison of a pair of images recorded with a small tilt of the specimen between the views (Finch, 1972). An iterative, real-space helical reconstruction method that uses single-particle processing procedures and offers an alternative to the Fourier–Bessel strategy has recently been developed and provides clear advantages for studying structures with imperfect helical symmetry (Egelman 2000, 2007*a,b*). Back-projection approaches offer a robust way of dealing with irregular helices or those with discontinuities or seams (Sosa & Milligan, 1996; Sosa *et al.*, 1997).

19.6.5.3. Icosahedral particles

The typical strategy for processing and 3D reconstruction of icosahedral particles consists of the following steps. First, a series of micrographs of a monodisperse distribution of particles,

normally suspended over holes in a perforated carbon support film, is recorded. After digitization of the micrographs, individual particle images are boxed and floated with a circular mask. The astigmatism and defocus of each micrograph is measured from the sum of intensities of the Fourier transforms of all particle images (Zhou *et al.*, 1996; Mallick *et al.*, 2005), or by a more automatic procedure applied to the whole micrograph (Mindell & Grigorieff, 2003). Auto-correlation techniques are then used to estimate the particle phase origins, which coincide with the centre of each particle where all rotational symmetry axes intersect (Olson & Baker, 1989). The view orientation of each particle, defined by three Eulerian angles, was originally determined by means of common and cross-common lines techniques (Crowther *et al.*, 1970; Crowther, 1971; Fuller *et al.*, 1996; Baker *et al.*, 1999; Thuman-Commike & Chiu, 2000), but is now more commonly determined with the aid of model-based, template-matching procedures (*e.g.* Baker & Cheng, 1996; Castón *et al.*, 1999; Grigorieff, 2007; Yan, Dryden *et al.*, 2007). Once a set of self-consistent particle images is available, an initial low-resolution 3D reconstruction is computed by merging these data with Fourier–Bessel (Crowther, 1971) or Fourier–Cartesian (*e.g.* Ji *et al.*, 2006) methods. This reconstruction then serves as a reference for refining the orientation, origin and CTF parameters of each of the included particle images, for rejecting 'bad' images, and for increasing the size of the data set by including new particle images from additional micrographs taken at different defocus levels. A new reconstruction, computed from the latest set of images, serves as a new reference and the above refinement procedure is repeated until no further improvements as measured by the reliability criteria mentioned above are made. Determination of the absolute hand of the structure requires the recording and processing of a pair of images taken with a known, small relative tilt of the specimen between the two views (Belnap *et al.*, 1997; Rosenthal & Henderson, 2003). In the past decade, 3D cryoTEM analysis of icosahedral viruses at sub-nanometre resolution has fully matured and near-atomic level (<4 Å) maps (*e.g.* Yu, Jin & Zhou, 2008; Zhang *et al.*, 2008; Zhou, 2008; Chen *et al.*, 2009) will certainly become more commonplace.

19.6.5.4. Electron cryo-tomography

This section is probably more appropriate to a cell-biology textbook than to *International Tables for Crystallography*, but we include it because of its growing importance and potential in the field of structural biology. Good reviews are to be found in Frank (2006*a*) and in three special issues of *Journal of Structural Biology* already mentioned in Table 19.6.5.1. Briefly, a tilt series of micrographs of the specimen is recorded, typically through an angular range of $\pm 60°$ or $\pm 70°$, and this is used, by *R*-weighted back projection, to produce a 3D map of the specimen. This can be further processed, segmented, coloured, rendered and interpreted (*e.g.* Medalia *et al.*, 2002; Nicastro *et al.*, 2005).

Electron cryo-tomography is typically used in two different ways. First, it is used to describe the structure of a unique, non-repeating biological sample such as a cell or organelle, possibly to observe how the structure can change or to explore the diversity of structures that occur. Second, it is used to produce a 3D map (tomogram) of a structure that includes many copies of identical assemblies, such as the trimeric glycoprotein surface spikes on HIV (*e.g.* Liu, Bartesaghi *et al.*, 2008). Individual 3D volumes are then selected from a number of tomograms to give several hundred or thousand sub-tomogram volumes, each of which contains a single copy of the object of interest viewed in an arbitrary direction. By averaging appropriately aligned 3D volumes, which represent a variety of orientations of presumed, identical structures, it is then possible to carry out the same type of averaging as described for all the other specimen types. Although the resolutions attained in the raw tomograms at present (~2009) range at best between 4 and 5 nm, and signal-to-noise considerations (Rosenthal & Henderson, 2003) suggest that the resolution of raw electron cryo-tomograms can never reach better than 1.5–2.0 nm, the procedure of sub-tomogram averaging of identical structures or substructures can, in principle, improve the resolution greatly. This second application of electron cryo-tomography thus fits perfectly into the context of *International Tables*. Examples of this application include the works by Fernandez *et al.* (2006), Zanetti *et al.* (2006), Liu, Bartesaghi *et al.* (2008), Zhu *et al.* (2008) and Zanetti *et al.* (2009). In the area of cellular tomography, the use of high-pressure freezing and cryo-sectioning followed by electron cryo-tomography is most promising (Zuber *et al.*, 2005, 2008; Salje *et al.*, 2009).

19.6.6. Visualization, modelling and interpretation of results

The explosive growth in the number of structures of macro-molecules and complexes that are now being determined at sub-nanometre resolutions has spawned the development of numerous tools that enable investigators to visualize, model and interpret their results. Generally, after assessing a global view of the gross morphology of a molecule, one quickly zooms in to explore finer and finer details. A major challenge, especially with density maps of increasing size (*e.g.* >512 pixels), is to perform these operations in real time. Several computer-graphics applications have emerged that satisfy a variety of requirements for visualizing cryoTEM maps. Examples of specific programs include *Chimera* (Pettersen *et al.*, 2004; Goddard *et al.*, 2005; Goddard & Ferrin, 2007; Goddard *et al.*, 2007), *colorRNA* (LeBarron *et al.*, 2007), *MODELLER* (Eswar *et al.*, 2007), *Python Molecular Viewer* (*PMV*) (Sanner, 1999; Gillet *et al.*, 2005), *Vision* (Sanner, 2005); *VMD* (Hsin *et al.*, 2008) and *VolRover* (Bajaj *et al.*, 2005). Many of these programs as well as most of the more common, multipurpose reconstruction programs provide tools for generating animations that can be used to help simulate data and that are particularly useful in communicating results to scientific as well as lay audiences (McGill, 2008). Additional useful tools allow one to produce space-filling, cartoon-like renderings of molecules that reduce unnecessary detail and hence are more easily understood (Goodsell, 2005).

Visualization tools merely provide an entryway to more careful scrutiny and interpretation of structure. When viewed in the context of existing biochemical and molecular studies as well as complementary X-ray crystallographic and other biophysical measurements, structural results provide a basis for understanding how molecules function. Even in the absence of complementary, high-resolution structural data, since 3D cryoTEM maps often reach sub-nanometre resolutions, it is usually possible to recognize characteristic, secondary structural elements like α-helices and large β-sheets in proteins. Several programs help identify such elements (Jiang, Baker *et al.*, 2001; Kong & Ma, 2003; Kong *et al.*, 2004; Baker *et al.*, 2007), and this then facilitates the process of defining and segmenting molecular envelopes (*e.g.* Volkmann, 2002; Baker, Yu *et al.*, 2006) and elucidating protein folds (Zhou *et al.*, 2001; Chiu *et al.*, 2002; Kovacs *et al.*, 2007; Lindert, Staritzbichler *et al.*, 2009). When
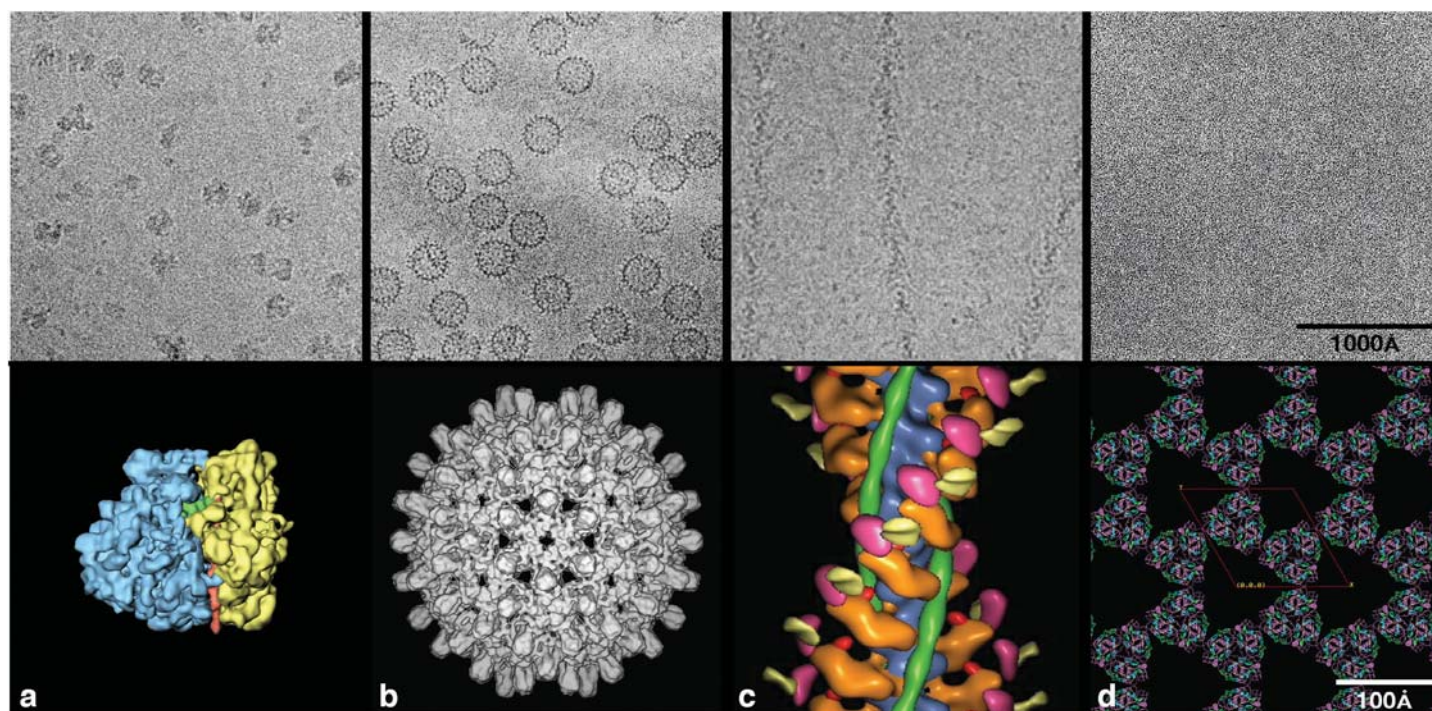
Figure 19.6.7.1
Examples of macromolecules studied by cryoTEM and 3D image reconstruction and the resulting 3D structures (bottom row) after cryoTEM analysis. All micrographs (top row) are displayed at ∼170 000× magnification and all models at ∼1 200 000× magnification. (*a*) A single particle without symmetry. The micrograph shows 70S *E. coli* ribosomes complexed with mRNA and fMet-tRNA. The surface-shaded density map, made by averaging 73 000 ribosome images from 287 micrographs, has a resolution of 11.5 Å. The 50S and 30S subunits and the tRNA are coloured blue, yellow and green, respectively. The identity of many of the protein and RNA components is known and some RNA double helices are clearly recognizable by their major and minor grooves (*e.g.* helix 44 is shown in red). Courtesy of J. Frank, using data from Gabashvili *et al.* (2000). (*b*) A single particle with symmetry. The micrograph shows hepatitis B virus cores. The 3D reconstruction, at a resolution of 7.4 Å, was computed from 6384 particle images taken from 34 micrographs. From Böttcher *et al.* (1997). (*c*) A helical filament. The micrograph shows actin filaments decorated with myosin S1 heads containing the essential light chain. The 3D reconstruction, at a resolution of 30–35 Å, is a composite in which the differently coloured parts are derived from a series of difference maps that were superimposed on F-actin. The components include: F-actin (blue), myosin heavy-chain motor domain (orange), essential light chain (purple), regulatory light chain (yellow), tropomyosin (green) and myosin motor domain N-terminal beta-barrel (magenta). Courtesy of A. Lin, M. Whittaker & R. Milligan (Scripps Research Institute, La Jolla). (*d*) A 2D crystal: light-harvesting complex LHCII at 3.4 Å resolution. The model shows the protein backbone and the arrangement of chromophores in a number of trimeric subunits in the crystal lattice. In this example, image contrast is too low to see any hint of the structure without image processing (see also Fig. 19.6.4.2). Courtesy of W. Kühlbrandt (Max-Planck-Institute for Biophysics, Frankfurt).

complementary data from X-ray crystallography are available for individual components of a macromolecule, or perhaps even the entire complex, so-called pseudo-atomic models can be produced that closely match the cryoTEM map and lead to more accurate and reliable data interpretation.

Pseudo-atomic models were originally constructed by docking X-ray-derived models manually into cryoTEM density maps (Wang *et al.*, 1992; Rayment *et al.*, 1993; Stewart *et al.*, 1993). However, qualitative procedures like these quickly spurred the development of rigorous, quantitative tools for fitting models into 3D maps as rigid bodies (Volkmann & Hanein, 1999; Wriggers *et al.*, 1999; Roseman, 2000; Rossmann *et al.*, 2001; Wriggers & Chacon, 2001; Chacón & Wriggers, 2002; Navaza *et al.*, 2002; Birmanns & Wriggers, 2003) and several of these methods have been the subject of review articles (Volkmann & Hanein, 2003; Fabiola & Chapman, 2005). The limitations inherent in assuming that vitrified molecules retain the same conformation found in crystals spawned the evolution of numerous flexible fitting and refinement methods (*e.g.* Wriggers & Birmanns, 2001; Gao & Frank, 2005; Velazquez-Muriel *et al.*, 2006; Tan *et al.*, 2008; Dimaio *et al.*, 2009). Many of the flexible fitting methods are based on normal-mode analysis (Tama *et al.*, 2003, 2004*a*,*b*; Bahar & Rader, 2005; Suhre *et al.*, 2006; Gorba *et al.*, 2008) and on molecular and damped dynamics (Kovacs *et al.*, 2008; Orze-

chowski & Tama, 2008; Trabuco *et al.*, 2008, 2009). When no X-ray structure is available to guide pseudo-atomic modelling of the cryoTEM map, it is still feasible to apply hybrid approaches (*e.g.* iterative structure-based sequence alignment, fitting and refinement) and construct a series of homology models (Topf *et al.*, 2005; Baker, Jiang *et al.*, 2006; Topf *et al.*, 2006; Lindert, Stewart & Meiler, 2009) that can be assessed to help identify reliable candidates (Shacham *et al.*, 2007; Velazquez-Muriel & Carazo, 2007).

19.6.7. Trends

The new generation of intermediate-voltage (∼300 kV) FEG microscopes with stable cold stages is now making it much easier to obtain higher-resolution images that, by use of larger defocus values, have good image contrast at both very low and very high resolution. The greater contrast at low resolution greatly facilitates particle-alignment procedures, and the increased contrast resulting from the high-coherence illumination helps to increase the signal-to-noise ratio for the structure at high resolution. Cold stages are constantly being improved, with several liquid-helium stages developed in the 1990s (Fujiyoshi *et al.*, 1991; Zemlin *et al.*, 1996). Two such stages are commercially available from JEOL and FEI.

Finally, some likely trends in the next few years include the following.

(1) Increased automation including:
  (*a*) specimen loading (Lefman *et al.*, 2007);
  (*b*) the recording of micrographs (Potter *et al.*, 1999; Zhang *et al.*, 2003; Lei & Frank, 2005; Suloway *et al.*, 2005; Zheng *et al.*, 2006; Nickell *et al.*, 2007; Yoshioka *et al.*, 2007; Shi *et al.*, 2008; Suloway *et al.*, 2009; Zhang *et al.*, 2009);
  (*c*) particle picking (Short, 2004; Zhu *et al.*, 2004; Chen & Grigorieff, 2007; Plaisier *et al.*, 2007; Woolford *et al.*, 2007; Sorzano *et al.*, 2009; Voss *et al.*, 2009), CTF estimation (*e.g.* Huang *et al.*, 2003; Fernando & Fuller, 2007; Jonic *et al.*, 2007; Sorzano *et al.*, 2007);
  (*d*) 3D reconstructions (*e.g.* Jiang, Li *et al.*, 2001; Mouche *et al.*, 2003; Stagg *et al.*, 2006; Yan, Sinkovits & Baker, 2007; Lander *et al.*, 2009); and
  (*e*) high-performance computing (*e.g.* Bilbao-Castro *et al.*, 2006; Castano-Diez *et al.*, 2007; Yang *et al.*, 2007; Castano-Diez *et al.*, 2008; Fernandez, 2008; Bilbao-Castro *et al.*, 2009).

(2) Introduction of better electronic cameras including:
  (*a*) lens-coupled CCDs (*e.g.* Maki-Yonekura & Yonekura, 2008);
  (*b*) complementary metal-oxide semiconductor (CMOS) sensors, which detect electrons directly. These are based on a technology used in many digital cameras and are displacing CCD technology for larger area detectors (Faruqi *et al.*, 2005; Milazzo *et al.*, 2005; Turchetta *et al.*, 2006; Xuong *et al.*, 2007; Jin *et al.*, 2008);
  (*c*) back-thinned CMOS sensors (McMullan, Faruqi *et al.*, 2009); and
  (*d*) silicon pixel detectors (*e.g.* Faruqi *et al.*, 2003; McMullan *et al.*, 2007).

(3) Increased use of dose-fractionated, tomographic tilt series to extend EM studies to the domain of larger supramolecular and cellular structures (*e.g.* McEwen *et al.*, 1995; Medalia *et al.*, 2002; Lucic *et al.*, 2005; Nicastro *et al.*, 2005, 2006; Jensen & Briegel, 2007; Zheng *et al.*, 2007; Salje *et al.*, 2009).

(4) Evaluation of C_c correctors for cryo-tomography of thicker specimens (Kabius *et al.*, 2009).

(5) The development and use of phase plates (*e.g.* Danev & Nagayama, 2001; Majorovits *et al.*, 2007; Danev & Nagayama, 2008; Nagayama & Danev, 2008; Danev *et al.*, 2009).

References

Adrian, M., Dubochet, J., Lepault, J. & McDowall, A. W. (1984). *Cryo-electron microscopy of viruses. Nature (London)*, **308**, 32–36.

Agard, D. A. (1983). *A least-squares method for determining structure factors in three-dimensional tilted-view reconstructions. J. Mol. Biol.* **167**, 849–852.

Agirrezabala, X., Martin-Benito, J., Valle, M., Gonzalez, J. M., Valencia, A., Valpuesta, J. M. & Carrascosa, J. L. (2005). *Structure of the connector of bacteriophage T7 at 8 Å resolution: structural homologies of a basic component of a DNA translocating machinery. J. Mol. Biol.* **347**, 895–902.

Amos, L. A., Henderson, R. & Unwin, P. N. T. (1982). *Three-dimensional structure determination by electron microscopy of two-dimensional crystals. Prog. Biophys. Mol. Biol.* **39**, 183–231.

Bahar, I. & Rader, A. J. (2005). *Coarse-grained normal mode analysis in structural biology. Curr. Opin. Struct. Biol.* **15**, 586–592.

Bajaj, C., Castrillon-Candas, J., Siddavanahalli, V. & Xu, Z. (2005). *Compressed representations of macromolecular structures and properties. Structure*, **13** 463–471.

Baker, M. L., Jiang, W., Wedemeyer, W. J., Rixon, F. J., Baker, D. & Chiu, W. (2006) *Ab initio modeling of the herpesvirus VP26 core domain assessed by CryoEM density. PLoS Comput. Biol.* **2**, e146.

Baker, M. L., Ju, T. & Chiu, W. (2007). *Identification of secondary structure elements in intermediate-resolution density maps. Structure*, **15**, 7–19.

Baker, M. L., Yu, Z., Chiu, W. & Bajaj, C. (2006). *Automated segmentation of molecular subunits in electron cryomicroscopy density maps. J. Struct. Biol.* **156**, 432–441.

Baker, T. S. & Cheng, R. H. (1996). *A model-based approach for determining orientations of biological macromolecules imaged by cryoelectron microscopy. J. Struct. Biol.* **116**, 120–130.

Baker, T. S., Olson, N. H. & Fuller, S. D. (1999). *Adding the third dimension to virus life cycles: three-dimensional reconstruction of icosahedral viruses from cryo-electron micrographs. Microbiol. Mol. Biol. Rev.* **63**, 862–922.

Baldwin, J. M., Henderson, R., Beckman, E. & Zemlin, F. (1988). *Images of purple membrane at 2.8 Å resolution obtained by cryo-electron microscopy. J. Mol. Biol.* **202**, 585–591.

Bárcena, M. & Koster, A. J. (2009). *Electron tomography in life science. Sem. Cell Develop. Biol.* **20**, 920–930.

Bartesaghi, A. & Subramaniam, S. (2009). *Membrane protein structure determination using cryo-electron tomography and 3D image averaging. Curr. Opin. Struct. Biol.* **19**, 402–407.

Baxter, W. T., Leith, A. & Frank, J. (2007). *SPIRE: the SPIDER reconstruction engine. J. Struct. Biol.* **157**, 56–63.

Bellare, J. R., Davis, H. T., Scriven, L. E. & Talmon, Y. (1988). *Controlled environment vitrification system: an improved sample preparation technique. J. Electron Microsc. Tech.* **10**, 87–111.

Belnap, D. M., Olson, N. H. & Baker, T. S. (1997). *A method for establishing the handedness of biological macromolecules. J. Struct. Biol.* **120**, 44–51.

Beroukhim, R. & Unwin, N. (1997). *Distortion correction of tubular crystals: improvements in the acetylcholine receptor structure. Ultra-microscopy*, **70**, 57–81.

Berriman, J. & Unwin, N. (1994). *Analysis of transient structures by cryo-microscopy combined with rapid mixing of spray droplets. Ultramicroscopy*, **56**, 241–252.

Beuron, F., Maurizi, M. R., Belnap, D. M., Kocsis, E., Booy, F. P., Kessel, M. & Steven, A. C. (1998). *At sixes and sevens: characterization and the symmetry mismatch of the ClpAP chaperone-assisted protease. J. Struct. Biol.* **123**, 248–259.

Bilbao-Castro, J. R., Carazo, J. M., Garcia, I. & Fernandez, J. J. (2006). *Parallelization of reconstruction algorithms in three-dimensional electron microscopy. Appl. Math. Model.* **30**, 688–701.

Bilbao-Castro, J. R., Marabini, R., Sorzano, C. O., Garcia, I., Carazo, J. M. & Fernandez, J. J. (2009). *Exploiting desktop supercomputing for three-dimensional electron microscopy reconstructions using ART with blobs. J. Struct. Biol.* **165**, 19–26.

Birmanns, S. & Wriggers, W. (2003). *Interactive fitting augmented by force-feedback and virtual reality. J. Struct. Biol.* **144**, 123–131.

Bloomer, A. C., Graham, J., Hovmoller, S., Butler, P. J. G. & Klug, A. (1978). *Protein disk of tobacco mosaic virus at 2.8 Å resolution showing the interactions within and between subunits. Nature (London)*, **276**, 362–368.

Booth, C. R., Jakana, J. & Chiu, W. (2006). *Assessing the capabilities of a 4k×4k CCD camera for electron cryo-microscopy at 300kV. J. Struct. Biol.* **156**, 556–563.

Booth, C. R., Jiang, W., Baker, M. L., Zhou, Z. H., Ludtke, S. J. & Chiu, W. (2004). *A 9 Å single particle reconstruction from CCD captured images on a 200 kV electron cryomicroscope. J. Struct. Biol.* **147**, 116–127.

Böttcher, B., Wynne, S. A. & Crowther, R. A. (1997). *Determination of the fold of the core protein of hepatitis B virus by electron microscopy. Nature (London)*, **386**, 88–91.

Brenner, S. & Horne, R. W. (1959). *A negative staining method for high resolution electron microscopy of viruses. Biochem. Biophys. Acta Protein Struct.* **34**, 103–110.

Brink, J., Sherman, M. B., Berriman, J. & Chiu, W. (1998). *Evaluation of charging on macromolecules in electron cryomicroscopy. Ultramicroscopy*, **72**, 41–52.

Burmeister, W. P. (2000). *Structural changes in a cryo-cooled protein crystal owing to radiation damage. Acta Cryst.* D**56**, 328–341.

Cantele, F., Lanzavecchia, S. & Bellon, P. L. (2003). *The variance of icosahedral virus models is a key indicator in the structure determination: a model-free reconstruction of viruses, suitable for refractory particles. J. Struct. Biol.* **141**, 84–92.

Carragher, B., Whittaker, M. & Milligan, R. A. (1996). *Helical processing using PHOELIX. J. Struct. Biol.* **116**, 107–112.

Carrascosa, J. L. & Steven, A. C. (1978). *A procedure for evaluation of significant structural differences between related arrays of protein molecules. Micron*, **9**, 199–206.

Castano-Diez, D., Moser, D., Schoenegger, A., Pruggnaller, S. & Frangakis, A. S. (2008). *Performance evaluation of image processing algorithms on the GPU. J. Struct. Biol.* **164**, 153–160.

Castano-Diez, D., Mueller, H. & Frangakis, A. S. (2007). *Implementation and performance evaluation of reconstruction algorithms on graphics processors. J. Struct. Biol.* **157**, 288–295.

Castón, J. R., Belnap, D. M., Steven, A. C. & Trus, B. L. (1999). *A strategy for determining the orientations of refractory particles for reconstruction from cryo-electron micrographs with particular reference to round, smooth-surfaced, icosahedral viruses. J. Struct. Biol.* **125**, 209–215.

Chacón, P. & Wriggers, W. (2002). *Multi-resolution contour-based fitting of macromolecular structures. J. Mol. Biol.* **317**, 375–384.

Chandramouli, P., Topf, M., Menetret, J. F., Eswar, N., Cannone, J. J., Gutell, R. R., Sali, A. & Akey, C. W. (2008). *Structure of the mammalian 80S ribosome at 8.7 Å resolution. Structure*, **16**, 535–548.

Chen, D. H., Jakana, J., Liu, X., Schmid, M. F. & Chiu, W. (2008). *Achievable resolution from images of biological specimens acquired from a 4k × 4k CCD camera in a 300-kV electron cryomicroscope. J. Struct. Biol.* **163**, 45–52.

Chen, J. Z. & Grigorieff, N. (2007). *SIGNATURE: a single-particle selection system for molecular electron microscopy. J. Struct. Biol.* **157**, 168–173.

Chen, J. Z., Settembre, E. C., Aoki, S. T., Zhang, X., Bellamy, A. R., Dormitzer, P. R., Harrison, S. C. & Grigorieff, N. (2009). *Molecular interactions in rotavirus assembly and uncoating seen by high-resolution cryo-EM. Proc. Natl Acad. Sci. USA*, **106**, 10644–10648.

Cheng, K., Koeck, P. J., Elmlund, H., Idakieva, K., Parvanova, K., Schwarz, H., Ternstrom, T. & Hebert, H. (2006). *Rapana thomasiana hemocyanin (RtH): comparison of the two isoforms, RtH1 and RtH2, at 19 Å and 16 Å resolution. Micron*, **37**, 566–576.

Cheng, R. H., Olson, N. H. & Baker, T. S. (1992). *Cauliflower mosaic virus, a 420 subunit (T = 7), multi-layer structure. Virology*, **186**, 655–668.

Cheng, Y. & Walz, T. (2009). *The advent of near-atomic resolution in single-particle electron microscopy. Annu. Rev. Biochem.* **78**, 723–742.

Cheng, Y., Zak, O., Aisen, P., Harrison, S. C. & Walz, T. (2004). *Structure of the human transferrin receptor–transferrin complex. Cell*, **116**, 565–576.

Chiu, W., Baker, M. L., Jiang, W., Dougherty, M. & Schmid, M. F. (2005). *Electron cryomicroscopy of biological machines at subnanometer resolution. Structure*, **13**, 363–372.

Chiu, W., Baker, M. L., Jiang, W. & Zhou, Z. H. (2002). *Deriving folds of macromolecular complexes through electron cryomicroscopy and bioinformatics approaches. Curr. Opin. Struct. Biol.* **12**, 263–269.

Conway, J. F. & Steven, A. C. (1999). *Methods for reconstructing density maps of 'single' particles from cryoelectron micrographs to subnanometer resolution. J. Struct. Biol.* **128**, 106–118.

Craig, L., Volkmann, N., Arvai, A. S., Pique, M. E., Yeager, M., Egelman, E. H. & Tainer, J. A. (2006). *Type IV pilus structure by cryo-electron microscopy and crystallography: implications for pilus assembly and functions. Mol. Cell*, **23**, 651–662.

Crewe, A. V. (1983). *High-resolution scanning transmission electron microscopy. Science*, **221**, 325–330.

Crowther, R. A. (1971). *Procedures for three-dimensional reconstruction of spherical viruses by Fourier synthesis from electron micrographs. Philos. Trans. R. Soc. London*, **261**, 221–230.

Crowther, R. A., Amos, L. A., Finch, J. T., DeRosier, D. J. & Klug, A. (1970). *Three dimensional reconstructions of spherical viruses by Fourier synthesis from electron micrographs. Nature (London)*, **226**, 421–425.

Crowther, R. A., Henderson, R. & Smith, J. M. (1996). *MRC image processing programs. J. Struct. Biol.* **116**, 9–16.

Crowther, R. A., Kiselev, N. A., Böttcher, B., Berriman, J. A., Borisova, G. P., Ose, V. & Pumpens, P. (1994). *Three-dimensional structure of hepatitis B virus core particles determined by electron cryomicroscopy. Cell*, **77**, 943–950.

Crowther, R. A. & Luther, P. K. (1984). *Three-dimensional reconstruction from a single oblique section of fish muscle M-band. Nature (London)*, **307**, 569–570.

Cyrklaff, M. & Kühlbrandt, W. (1994). *High resolution electron microscopy of biological specimens in cubic ice. Ultramicroscopy*, **55**, 141–153.

Danev, R., Glaeser, R. M. & Nagayama, K. (2009). *Practical factors affecting the performance of a thin-film phase plate for transmission electron microscopy. Ultramicroscopy*, **109**, 312–325.

Danev, R. & Nagayama, K. (2001). *Transmission electron microscopy with Zernike phase plate. Ultramicroscopy*, **88**, 243–252.

Danev, R. & Nagayama, K. (2008). *Single particle analysis based on Zernike phase contrast transmission electron microscopy. J. Struct. Biol.* **161**, 211–218.

Dang, T. X., Farah, S. J., Gast, A., Robertson, C., Carragher, B., Egelman, E. & Wilson-Kubalek, E. M. (2005). *Helical crystallization on lipid nanotubes: streptavidin as a model protein. J. Struct. Biol.* **150**, 90–99.

DeRosier, D. J. & Klug, A. (1968). *Reconstruction of three dimensional structures from electron micrographs. Nature (London)*, **217**, 130–134.

DeRosier, D. J. & Moore, P. B. (1970). *Reconstruction of three-dimensional images from electron micrographs of structures with helical symmetry. J. Mol. Biol.* **52**, 355–369.

Dimaio, F., Tyka, M. D., Baker, M. L., Chiu, W. & Baker, D. (2009). *Refinement of protein structures into low-resolution density maps using Rosetta. J. Mol. Biol.* **392**, 181–190.

Dubochet, J., Adrian, M., Chang, J.-J., Homo, J.-C., Lepault, J., McDowall, A. W. & Schultz, P. (1988). *Cryo-electron microscopy of vitrified specimens. Q. Rev. Biophys.* **21**, 129–228.

Dubochet, J., Lepault, J., Freeman, R., Berriman, J. A. & Homo, J.-C. (1982). *Electron microscopy of frozen water and aqueous solutions. J. Microsc.* **128**, 219–237.

Egelman, E. H. (1986). *An algorithm for straightening images of curved filamentous structures. Ultramicroscopy*, **19**, 367–374.

Egelman, E. H. (2000). *A robust algorithm for the reconstruction of helical filaments using single-particle methods. Ultramicroscopy*, **85**, 225–234.

Egelman, E. H. (2007a). *The iterative helical real space reconstruction method: surmounting the problems posed by real polymers. J. Struct. Biol.* **157**, 83–94.

Egelman, E. H. (2007b). *Single-particle reconstruction from EM images of helical filaments. Curr. Opin. Struct. Biol.* **17**, 556–561.

Elmlund, H., Lundqvist, J. , Al-Karadaghi, S., Hansson, M., Hebert, H. & Lindahl, M. (2008). *A new cryo-EM single-particle ab initio reconstruction method visualizes secondary structure elements in an ATP-fueled AAA+ motor. J. Mol. Biol.* **375**, 934–947.

Erickson, H. P. & Klug, A. (1971). *Measurement and compensation of defocusing and aberrations by Fourier processing of micrographs. Philos. Trans. R. Soc. London Ser. B*, **261**, 105–118.

Eswar, N., Webb, B., Marti-Renom, M. A., Madhusudhan, M. S., Eramian, D., Shen, M. Y., Pieper, U. & Sali, A. (2007). *Comparative protein structure modeling using MODELLER. Curr. Protoc. Protein Sci.* ch. 2, unit 2.9.

Fabiola, F. & Chapman, M. S. (2005). *Fitting of high-resolution structures into electron microscopy reconstruction images. Structure*, **13**, 389–400.

Faruqi, A. R., Cattermole, D. M. & Raeburn, C. (2003). *Direct electron detection methods in electron microscopy. Nucl. Instrum. Methods Phys. Res. A*, **513**, 317–321.

Faruqi, A. R., Henderson, R., Pryddetch, M., Allport, P. & Evans, A. (2005). *Direct single electron detection with a CMOS detector for electron microscopy. Nucl. Instrum. Methods Phys. Res. A*, **546**, 170–175.

Fernandez, J. J. (2008). *High performance computing in structural determination by electron cryomicroscopy. J. Struct. Biol.* **164**, 1–6.

Fernandez, J. J., Li, S. & Crowther, R. A. (2006). *CTF determination and correction in electron cryotomography. Ultramicroscopy*, **106**, 587–596.

Fernandez, J. J., Luque, D., Caston, J. R. & Carrascosa, J. L. (2008). *Sharpening high resolution information in single particle electron cryomicroscopy*. J. Struct. Biol. **164**, 170–175.

Fernandez-Tornero, C., Bottcher, B., Riva, M., Carles, C., Steuerwald, U., Ruigrok, R. W., Sentenac, A., Muller, C. W. & Schoehn, G. (2007). *Insights into transcription initiation and termination from the electron microscopy structure of yeast RNA polymerase III*. Mol. Cell, **25**, 813–823.

Fernando, K. V. & Fuller, S. D. (2007). *Determination of astigmatism in TEM images*. J. Struct. Biol. **157**, 189–200.

Finch, J. T. (1972). *The hand of the helix of tobacco mosaic virus*. J. Mol. Biol. **66**, 291–294.

Fleishman, S. J., Unger, V. M., Yeager, M. & Ben-Tal, N. (2004). *A Calpha model for the transmembrane alpha helices of gap junction intercellular channels*. Mol. Cell, **15**, 879–888.

Ford, R. C., Brunkan-LaMontagne, A. L., Collins, R. F., Clarke, B. R., Harris, R., Naismith, J. H. & Whitfield, C. (2009). *Structure-function relationships of the outer membrane translocon Wza investigated by cryo-electron microscopy and mutagenesis*. J. Struct. Biol. **166**, 172–182.

Fotin, A., Cheng, Y., Sliz, P., Grigorieff, N., Harrison, S. C., Kirchhausen, T. & Walz, T. (2004). *Molecular model for a complete clathrin lattice from electron cryomicroscopy*. Nature (London), **432**, 573–579.

Frank, J. (2002). *Single-particle imaging of macromolecules by cryo-electron microscopy*. Annu. Rev. Biophys. Biomol. Struct. **31**, 303–319.

Frank, J. (2006a). Editor. *Electron Tomography: Methods for Three-Dimensional Visualization of Structures in the Cell*. New York: Springer.

Frank, J. (2006b). *Three-Dimensional Electron Microscopy of Macromolecular Assemblies: Visualization of Biological Molecules in their Native State*. Oxford University Press.

Frank, J., Radermacher, M., Penczek, P., Zhu, J., Li, Y., Ladjadj, M. & Leith, A. (1996). *SPIDER and WEB: processing and visualization of images in 3D electron microscopy and related fields*. J. Struct. Biol. **116**, 190–199.

Frank, J., Verschoor, A. & Boublik, M. (1981). *Computer averaging of electron micrographs of 40S ribosomal subunits*. Science, **214**, 1353–1355.

Frost, A., Perera, R., Roux, A., Spasov, K., Destaing, O., Egelman, E. H., De Camilli, P. & Unger, V. M. (2008). *Structural basis of membrane invagination by F-BAR domains*. Cell, **132**, 807–817.

Fujiyoshi, Y., Mizusaki, T., Morikawa, K., Yamagishi, H., Aoki, Y., Kihara, H. & Harada, Y. (1991). *Development of a superfluid helium stage for high-resolution electron microscopy*. Ultramicroscopy, **38**, 241–251.

Fuller, S. D., Berriman, J. A., Butcher, S. J. & Gowen, B. E. (1995). *Low pH induces swiveling of the glycoprotein heterodimers in the Semiliki forest virus spike complex*. Cell, **81**, 715–725.

Fuller, S. D., Butcher, S. J., Cheng, R. H. & Baker, T. S. (1996). *Three-dimensional reconstruction of icosahedral particles – the uncommon line*. J. Struct. Biol. **116**, 48–55.

Fung, J. C., Liu, W., DeRuijter, W. J., Chen, H., Abbey, C. K., Sedat, J. W. & Agard, D. A. (1996). *Toward fully automated high-resolution electron tomography*. J. Struct. Biol. **116**, 181–189.

Gabashvili, I. S., Agrawal, R. K., Spahn, C. M. T., Grassucci, R. A., Svergun, D. I., Frank, J. & Penczek, P. (2000). *Solution structure of the E. coli 70S ribosome at 11.5 Å resolution*. Cell, **100**, 537–549.

Galkin, V. E., Orlova, A., Cherepanova, O., Lebart, M. C. & Egelman, E. H. (2008). *High-resolution cryo-EM structure of the F-actin–fimbrin/plastin ABD2 complex*. Proc. Natl Acad. Sci. USA, **105**, 1494–1498.

Gao, H. & Frank, J. (2005). *Molding atomic structures into intermediate-resolution cryo-EM density maps of ribosomal complexes using real-space refinement*. Structure, **13**, 401–406.

Gatsogiannis, C., Moeller, A., Depoix, F., Meissner, U. & Markl, J. (2007). *Nautilus pompilius hemocyanin: 9 Å cryo-EM structure and molecular model reveal the subunit pathway and the interfaces between the 70 functional units*. J. Mol. Biol. **374**, 465–486.

Gillet, A., Sanner, M., Stoffler, D. & Olson, A. (2005). *Tangible interfaces for structural molecular biology*. Structure, **13**, 483–491.

Gipson, B., Zeng, X. & Stahlberg, H. (2007). *2dx_merge: data management and merging for 2D crystal images*. J. Struct. Biol. **160**, 375–384.

Gipson, B., Zeng, X., Zhang, Z. Y. & Stahlberg, H. (2007). *2dx – user-friendly image processing for 2D crystals*. J. Struct. Biol. **157**, 64–72.

Glaeser, R., Downing, K., DeRosier, D., Chiu, W. & Frank, J. (2007). *Electron Crystallography of Biological Macromolecules*. Oxford University Press.

Glaeser, R. M. (1971). *Limitations to significant information in biological electron microscopy as a result of radiation damage*. J. Ultrastruct. Res. **36**, 466–482.

Glaeser, R. M. (2008a). *Cryo-electron microscopy of biological nanostructures*. Phys. Today, **61**, 48–54.

Glaeser, R. M. (2008b). *Retrospective: radiation damage and its associated 'information limitations'*. J. Struct. Biol. **163**, 271–276.

Goddard, T. D. & Ferrin, T. E. (2007). *Visualization software for molecular assemblies*. Curr. Opin. Struct. Biol. **17**, 587–595.

Goddard, T. D., Huang, C. C. & Ferrin, T. E. (2005). *Software extensions to UCSF chimera for interactive visualization of large molecular assemblies*. Structure, **13**, 473–482.

Goddard, T. D., Huang, C. C. & Ferrin, T. E. (2007). *Visualizing density maps with UCSF Chimera*. J. Struct. Biol. **157**, 281–287.

Gonen, T., Cheng, Y., Sliz, P., Hiroaki, Y., Fujiyoshi, Y., Harrison, S. C. & Walz, T. (2005). *Lipid–protein interactions in double-layered two-dimensional AQP0 crystals*. Nature (London), **438**, 633–638.

Goodsell, D. S. (2005). *Visual methods from atoms to cells*. Structure, **13**, 347–354.

Gorba, C., Miyashita, O. & Tama, F. (2008). *Normal-mode flexible fitting of high-resolution structure of biological molecules toward one-dimensional low-resolution data*. Biophys. J. **94**, 1589–1599.

Grant, R. A., Filman, D. J., Finkel, S. E., Kolter, R. & Hogle, J. M. (1998). *The crystal structure of Dps, a ferritin homolog that binds and protects DNA*. Nat. Struct. Biol. **5**, 294–303.

Grassucci, R. A., Taylor, D. J. & Frank, J. (2007). *Preparation of macromolecular complexes for cryo-electron microscopy*. Nat. Protoc. **2**, 3239–3246.

Gregorini, M., Wang, J., Xie, X. S., Milligan, R. A. & Engel, A. (2007). *Three-dimensional reconstruction of bovine brain V-ATPase by cryo-electron microscopy and single particle analysis*. J. Struct. Biol. **158**, 445–454.

Grigorieff, N. (1998). *Three-dimensional structure of bovine NADH: ubiquinone oxidoreductase (complex I) at 22 Å in ice*. J. Mol. Biol. **277**, 1033–1046.

Grigorieff, N. (2007). *FREALIGN: high-resolution refinement of single particle structures*. J. Struct. Biol. **157**, 117–125.

Hall, R. J., Siridechadilok, B. & Nogales, E. (2007). *Cross-correlation of common lines: a novel approach for single-particle reconstruction of a structure containing a flexible domain*. J. Struct. Biol. **159**, 474–482.

Hardt, S., Wang, B. & Schmid, M. F. (1996). *A brief description of I.C.E.: the integrated crystallographic environment*. J. Struct. Biol. **116**, 68–70.

Hargittai, I. & Hargittai, M. (1988). Editors. *Stereochemical Applications of Gas-Phase Electron Diffraction*. New York: VCH.

Hasler, L., Heymann, J. B., Engel, A., Kistler, J. & Walz, T. (1998). *2D crystallization of membrane proteins: rationales and examples*. J. Struct. Biol. **121**, 162–171.

Havelka, W. A., Henderson, R. & Oesterhelt, D. (1995). *Three-dimensional structure of halorhodopsin at 7 Å resolution*. J. Mol. Biol. **247**, 726–738.

He, Y. & Olson, R. (2010). *Three-dimensional structure of the detergent-solubilized Vibrio cholerae cytolysin (VCC) heptamer by electron cryomicroscopy*. J. Struct. Biol. **169**, 6–13.

Heel, M. van (1987a). *Angular reconstitution: a posteriori assignment of projection directions for 3D reconstruction*. Ultramicroscopy, **21**, 111–124.

Heel, M. van (1987b). *Similarity measures between images*. Ultramicroscopy, **21**, 95–100.

Heel, M. van & Frank, J. (1981). *Use of multivariate statistics in analyzing the images of biological macromolecules*. Ultramicroscopy, **6**, 187–194.

Heel, M. van, Gowen, B., Matadeen, R., Orlova, E. V., Finn, R., Pape, T., Cohen, D., Stark, H., Schmidt, R., Schatz, M. & Patwardhan, A. (2000). *Single-particle electron cryo-microscopy: towards atomic resolution*. Quart. Rev. Biophys. **33**, 307–369.

Heel, M. van, Harauz, G. & Orlova, E. V. (1996). *A new generation of the IMAGIC image processing system*. J. Struct. Biol. **116**, 17–24.

Heel, M. van & Hollenberg, J. (1980). *On the stretching of distorted images of two-dimensional crystals*. In *Electron Microscopy at Molecular Dimensions*, edited by W. Baumeister & W. Vogell, pp. 256–260. Berlin: Springer-Verlag.

Heitkamp, T., Bottcher, B. & Greie, J. C. (2009). *Solution structure of the KdpFABC P-type ATPase from Escherichia coli by electron microscopic single particle analysis*. J. Struct. Biol. **166**, 295–302.

Henderson, R. (1995). *The potential and limitations of neutrons, electrons, and X-rays for atomic resolution microscopy of unstained biological molecules. Q. Rev. Biophys.* **28**, 171–193.

Henderson, R. (2004). *Realizing the potential of electron cryomicroscopy. Quart. Rev. Biophys.* **37**, 3–13.

Henderson, R., Baldwin, J. M., Ceska, T. A., Zemlin, F., Beckmann, E. & Downing, K. H. (1990). *Model for the structure of bacteriorhodopsin based on high-resolution electron cryo-microscopy. J. Mol. Biol.* **213**, 899–929.

Henderson, R., Baldwin, J. M., Downing, K. H., Lepault, J. & Zemlin, F. (1986). *Structure of purple membrane from halobacterium: recording, measurement, and evaluation of electron micrographs at 3.5 Å resolution. Ultramicroscopy*, **19**, 147–178.

Henderson, R. & Unwin, P. N. T. (1975). *Three-dimensional model of purple membrane obtained by electron microscopy. Nature (London)*, **257**, 28–32.

Hite, R. K., Raunser, S. & Walz, T. (2007). *Revival of electron crystallography. Curr. Opin. Struct. Biol.* **17**, 389–395.

Hoenger, A. & McIntosh, J. R. (2009). *Probing the macromolecular organization of cells by electron tomography. Curr. Opin. Cell Biol.* **21**, 89–96.

Holm, P. J., Bhakat, P., Jegerschold, C., Gyobu, N., Mitsuoka, K., Fujiyoshi, Y., Morgenstern, R. & Hebert, H. (2006). *Structural basis for detoxification and oxidative stress protection in membranes. J. Mol. Biol.* **360**, 934–945.

Hoppe, W., Langer, R., Knesch, G. & Poppe, C. (1968). *Protein-kristallstrukturanalyse mit elektronenstrahlen. Naturwissenschaften*, **55**, 333–336.

Hsin, J., Arkhipov, A., Yin, Y., Stone, J. E. & Schulten, K. (2008). *Using VMD: an introductory tutorial. Curr. Protoc. Bioinfor.* ch. 5, unit 5.7.

Huang, Z., Baldwin, P. R., Mullapudi, S. & Penczek, P. A. (2003). *Automated determination of parameters describing power spectra of micrograph images in electron microscopy. J. Struct. Biol.* **144**, 79–94.

Huxley, H. E. & Zubay, G. (1960). *Electron microscope observations on the structure of microsomal particles from Escherichia coli. J. Mol. Biol.* **2**, 10–18.

Iancu, C. V., Tivol, W. F., Schooler, J. B., Dias, D. P., Henderson, G. P., Murphy, G. E., Wright, E. R., Li, Z., Yu, Z., Briegel, A., Gan, L., He, Y. & Jensen, G. J. (2006). *Electron cryotomography sample preparation using the Vitrobot. Nat. Protoc.* **1**, 2813–2819.

Isaacson, M., Langmore, J. & Rose, H. (1974). *Determination of the non-localization of the inelastic scattering of electrons by electron microscopy. Optik*, **41**, 92–96.

Jap, B., Zulauf, M., Scheybani, T., Hefti, A., Baumeister, W. & Aebi, U. (1992). *2D crystallization: from art to science. Ultramicroscopy*, **46**, 45–84.

Jegerschold, C., Pawelzik, S. C., Purhonen, P., Bhakat, P., Gheorghe, K. R., Gyobu, N., Mitsuoka, K., Morgenstern, R., Jakobsson, P. J. & Hebert, H. (2008). *Structural basis for induced formation of the inflammatory mediator prostaglandin E2. Proc. Natl Acad. Sci. USA*, **105**, 11110–11115.

Jensen, G. J. & Briegel, A. (2007). *How electron cryotomography is opening a new window onto prokaryotic ultrastructure. Curr. Opin. Struct. Biol.* **17**, 260–267.

Ji, Y., Marinescu, D. C., Zhang, W., Zhang, X., Yan, X. & Baker, T. S. (2006). *A model-based parallel origin and orientation refinement algorithm for cryoTEM and its application to the study of virus structures. J. Struct. Biol.* **154**, 1–19.

Jiang, W., Baker, M. L., Jakana, J., Weigele, P. R., King, J. & Chiu, W. (2008). *Backbone structure of the infectious epsilon15 virus capsid revealed by electron cryomicroscopy. Nature (London)*, **451**, 1130–1134.

Jiang, W., Baker, M. L., Ludtke, S. J. & Chiu, W. (2001). *Bridging the information gap: computational tools for intermediate resolution structure interpretation. J. Mol. Biol.* **308**, 1033–1044.

Jiang, W., Li, Z., Zhang, Z., Booth, C. R., Baker, M. L. & Chiu, W. (2001). *Semi-automated icosahedral particle reconstruction at sub-nanometer resolution. J. Struct. Biol.* **136**, 214–225.

Jin, L., Milazzo, A. C., Kleinfelder, S., Li, S., Leblanc, P., Duttweiler, F., Bouwer, J. C., Peltier, S. T., Ellisman, M. H. & Xuong, N. H. (2008). *Applications of direct detection device in transmission electron microscopy. J. Struct. Biol.* **161**, 352–358.

Jonic, S., Sorzano, C. O. & Boisset, N. (2008). *Comparison of single-particle analysis and electron tomography approaches: an overview. J. Microsc.* **232**, 562–579.

Jonic, S., Sorzano, C. O., Cottevieille, M., Larquet, E. & Boisset, N. (2007). *A novel method for improvement of visualization of power spectra for sorting cryo-electron micrographs and their local areas. J. Struct. Biol.* **157**, 156–167.

Kabius, B., Hartel, P., Haider, M., Muller, H., Uhlemann, S., Loebau, U., Zach, J. & Rose, H. (2009). *First application of Cc-corrected imaging for high-resolution and energy-filtered TEM. J. Electron Microsc.* **58**, 147–155.

Kasas, S., Dumas, G., Dietler, G., Catsicas, S. & Adrian, M. (2003). *Vitrification of cryoelectron microscopy specimens revealed by high-speed photographic imaging. J. Microsc.* **211**, 48–53.

Kenney, J., Karsenti, E., Gowen, B. & Fuller, S. D. (1997). *Three-dimensional reconstruction of the mammalian centriole from cryoelectron micrographs: the use of common lines for orientation and alignment. J. Struct. Biol.* **120**, 320–328.

Klug, A. & Berger, J. E. (1964). *An optical method for the analysis of periodicities in electron micrographs, and some observations on the mechanism of negative staining. J. Mol. Biol.* **10**, 565–569.

Klug, A. & DeRosier, D. J. (1966). *Optical filtering of electron micrographs: reconstruction of one sided images. Nature (London)*, **212**, 29–32.

Koeck, P. J., Purhonen, P., Alvang, R., Grundberg, B. & Hebert, H. (2007). *Single particle refinement in electron crystallography: a pilot study. J. Struct. Biol.* **160**, 344–352.

Kong, Y. & Ma, J. (2003). *A structural-informatics approach for mining β-sheets: locating sheets in intermediate-resolution density maps. J. Mol. Biol.* **332**, 399–413.

Kong, Y., Zhang, X., Baker, T. S. & Ma, J. (2004). *A structural-informatics approach for tracing β-sheets: building pseudo-Cα traces for β-strands in intermediate-resolution density maps. J. Mol. Biol.* **339**, 117–130.

Kornberg, R. & Darst, S. A. (1991). *Two dimensional crystals of proteins on liquid layers. Curr. Opin. Struct. Biol.* **1**, 642–646.

Kovacs, J. A., Yeager, M. & Abagyan, R. (2007). *Computational prediction of atomic structures of helical membrane proteins aided by EM maps. Biophys. J.* **93**, 1950–1959.

Kovacs, J. A., Yeager, M. & Abagyan, R. (2008). *Damped-dynamics flexible fitting. Biophys. J.* **95**, 3192–3207.

Krivanek, O. L. & Mooney, P. E. (1993). *Applications of slow-scan CCD cameras in transmission electron microscopy. Ultramicroscopy*, **49**, 95–108.

Kubalek, E. W., LeGrice, S. F. J. & Brown, P. O. (1994). *Two-dimensional crystallization of histidine-tagged, HIV-1 reverse transcriptase promoted by a novel nickel-chelating lipid. J. Struct. Biol.* **113**, 117–123.

Kühlbrandt, W., Wang, D. N. & Fujiyoshi, Y. (1994). *Atomic model of plant light-harvesting complex by electron crystallography. Nature (London)*, **367**, 614–621.

Kunji, E. R., von Gronau, S., Oesterhelt, D. & Henderson, R. (2000). *The three-dimensional structure of halorhodopsin to 5 Å by electron crystallography: a new unbending procedure for two-dimensional crystals by using a global reference structure. Proc. Natl Acad. Sci. USA*, **97**, 4637–4642.

Lander, G. C., Stagg, S. M., Voss, N. R., Cheng, A., Fellmann, D., Pulokas, J., Yoshioka, C., Irving, C., Mulder, A., Lau, P. W., Lyumkis, D., Potter, C. S. & Carragher, B. (2009). *Appion: an integrated, database-driven pipeline to facilitate EM image processing. J. Struct. Biol.* **166**, 95–102.

Landsberg, M. J. & Hankamer, B. (2007). *Symmetry: a guide to its application in 2D electron crystallography. J. Struct. Biol.* **160**, 332–343.

Lau, W. C., Baker, L. A. & Rubinstein, J. L. (2008). *Cryo-EM structure of the yeast ATP synthase. J. Mol. Biol.* **382**, 1256–1264.

Lawton, J. A. & Prasad, B. V. V. (1996). *Automated software package for icosahedral virus reconstruction. J. Struct. Biol.* **116**, 209–215.

LeBarron, J., Grassucci, R. A., Shaikh, T. R., Baxter, W. T., Sengupta, J. & Frank, J. (2008). *Exploration of parameters in cryo-EM leading to an improved density map of the E. coli ribosome. J. Struct. Biol.* **164**, 24–32.

LeBarron, J., Mitra, K. & Frank, J. (2007). *Displaying 3D data on RNA secondary structures: coloRNA. J. Struct. Biol.* **157**, 262–270.

Lefman, J., Morrison, R. & Subramaniam, S. (2007). *Automated 100-position specimen loader and image acquisition system for transmission electron microscopy. J. Struct. Biol.* **158**, 318–326.

Lei, J. & Frank, J. (2005). *Automated acquisition of cryo-electron micrographs for single particle reconstruction on an FEI Tecnai electron microscope. J. Struct. Biol.* **150**, 69–80.

Leis, A., Rockel, B., Andrees, L. & Baumeister, W. (2009). *Visualizing cells at the nanoscale. Trends Biochem. Sci.* **34**, 60–70.

Leschziner, A. E. & Nogales, E. (2006). *The orthogonal tilt reconstruction method: an approach to generating single-class volumes with no missing cone for ab initio reconstruction of asymmetric particles*. *J. Struct. Biol.* **153**, 284–299.

Li, H., DeRosier, D. J., Nicholson, W. V., Nogales, E. & Downing, K. H. (2002). *Microtubule structure at 8 Å resolution*. *Structure*, **10**, 1317–1328.

Li, Z. & Jensen, G. J. (2009). *Electron cryotomography: a new view into microbial ultrastructure*. *Curr. Opin. Microbiol.* **12**, 333–340.

Liang, Y., Ke, E. Y. & Zhou, Z. H. (2002). *IMIRS: a high-resolution 3D reconstruction package integrated with a relational image database*. *J. Struct. Biol.* **137**, 292–304.

Lindert, S., Staritzbichler, R., Wotzel, N., Karakas, M., Stewart, P. L. & Meiler, J. (2009). *EM-fold: De novo folding of alpha-helical proteins guided by intermediate-resolution electron microscopy density maps*. *Structure*, **17**, 990–1003.

Lindert, S., Stewart, P. L. & Meiler, J. (2009). *Hybrid approaches: applying computational methods in cryo-electron microscopy*. *Curr. Opin. Struct. Biol.* **19**, 218–225.

Liu, H., Cheng, L., Zeng, S., Cai, C., Zhou, Z. H. & Yang, Q. (2008). *Symmetry-adapted spherical harmonics method for high-resolution 3D single-particle reconstructions*. *J. Struct. Biol.* **161**, 64–73.

Liu, J., Bartesaghi, A., Borgnia, M. J., Sapiro, G. & Subramaniam, S. (2008). *Molecular architecture of native HIV-1 gp120 trimers. Nature (London)*, **455**, 109–113.

Liu, J., Wu, S., Reedy, M. C., Winkler, H., Lucaveche, C., Cheng, Y., Reedy, M. K. & Taylor, K. A. (2006). *Electron tomography of swollen rigor fibers of insect flight muscle reveals a short and variably angled S2 domain. J. Mol. Biol.* **362**, 844–860.

Liu, X., Jiang, W., Jakana, J. & Chiu, W. (2007). *Averaging tens to hundreds of icosahedral particle images to resolve protein secondary structure elements using a multi-path simulated annealing optimization algorithm. J. Struct. Biol.* **160**, 11–27.

Lucic, V., Forster, F. & Baumeister, W. (2005). *Structural studies by electron tomography: from cells to molecules. Annu. Rev. Biochem.* **74**, 833–865.

Ludtke, S. J., Baker, M. L., Chen, D. H., Song, J. L., Chuang, D. T. & Chiu, W. (2008). *De novo backbone trace of GroEL from single particle electron cryomicroscopy. Structure*, **16**, 441–448.

Ludtke, S. J., Baldwin, P. R. & Chiu, W. (1999). *EMAN: semiautomated software for high-resolution single-particle reconstructions. J. Struct. Biol.* **128**, 82–97.

Ludtke, S. J., Serysheva, I. I., Hamilton, S. L. & Chiu, W. (2005). *The pore structure of the closed RyR1 channel. Structure*, **13**, 1203–1211.

McEwen, B. F., Downing, K. H. & Glaeser, R. M. (1995). *The relevance of dose-fractionation in tomography of radiation-sensitive specimens. Ultramicroscopy*, **60**, 357–373.

McEwen, B. F., Renken, C., Marko, M. & Mannella, C. (2008). *Chapter 6: Principles and practice in electron tomography. Methods Cell Biol.* **89**, 129–168.

McGill, G. (2008). *Molecular movies . . . coming to a lecture near you. Cell*, **133**, 1127–1132.

McMullan, G., Cattermole, D. M., Chen, S., Henderson, R., Llopart, X., Summerfield, C., Tlustos, L. & Faruqi, A. R. (2007). *Electron imaging with Medipix2 hybrid pixel detector. Ultramicroscopy*, **107**, 401–413.

McMullan, G., Chen, S., Henderson, R. & Faruqi, A. R. (2009). *Detective quantum efficiency of electron area detectors in electron microscopy. Ultramicroscopy*, **109**, 1126–1143.

McMullan, G., Faruqi, A. R., Henderson, R., Guerrini, N., Turchetta, R., Jacobs, A. & van Hoften, G. (2009). *Experimental observation of the improvement in MTF from backthinning a CMOS direct electron detector. Ultramicroscopy*, **109**, 1144–1147.

Majorovits, E., Barton, B., Schultheiss, K., Perez-Willard, F., Gerthsen, D. & Schroder, R. R. (2007). *Optimizing phase contrast in transmission electron microscopy with an electrostatic (Boersch) phase plate. Ultramicroscopy*, **107**, 213–226.

Maki-Yonekura, S. & Yonekura, K. (2008). *Electron digital imaging toward high-resolution structure analysis of biological macromolecules. Microsc. Microanal.* **14**, 362–369.

Mallick, S. P., Carragher, B., Potter, C. S. & Kriegman, D. J. (2005). *ACE: automated CTF estimation. Ultramicroscopy*, **104**, 8–29.

Mancini, E. J., de Haas, F. & Fuller, S. D. (1997). *High-resolution icosahedral reconstruction: fulfilling the promise of cryo-electron microscopy. Structure*, **5**, 741–750.

Marlovits, T. C., Kubori, T., Lara-Tejero, M., Thomas, D., Unger, V. M. & Galan, J. E. (2006). *Assembly of the inner rod determines needle length in the type III secretion injectisome. Nature (London)*, **441**, 637–640.

Mastronarde, D. N. (2005). *Automated electron microscope tomography using robust prediction of specimen movements. J. Struct. Biol.* **152**, 36–51.

Matadeen, R., Hon, W. C., Heath, J. K., Jones, E. Y. & Fuller, S. (2007). *The dynamics of signal triggering in a gp130-receptor complex. Structure*, **15**, 441–448.

Mattevi, A., Obmolova, G., Schulze, E., Kalk, K. H., Westphal, A. H., de Kok, A. & Hol, W. G. J. (1992). *Atomic structure of the cubic core of the pyruvate dehydrogenase multienzyme complex. Science*, **255**, 1544–1550.

Mayer, E. & Astl, G. (1992). *Limits of cryofixation as seen by Fourier transform infrared spectra of metmyoglobin azide and carbonyl hemoglobin in vitrified and freeze concentrated aqueous solution. Ultramicroscopy*, **45**, 185–197.

Medalia, O., Weber, I., Frangakis, A. S., Nicastro, D., Gerisch, G. & Baumeister, W. (2002). *Macromolecular architecture in eukaryotic cells visualized by cryoelectron tomography. Science*, **298**, 1209–1213.

Meents, A., Gutmann, S., Wagner, A. & Schulze-Briese, C. (2010). *Origin and temperature dependence of radiation damage in biological samples at cryogenic temperatures. Proc. Natl Acad. Sci. USA*, **107**, 1094–1099.

Melanson, L. (2009). *A versatile and affordable plunge freezing instrument for preparing frozen hydrated specimens for cryo transmission electron microscopy (CryoEM). Microsc. Today*, **17**, 14–17.

Meng, X., Wang, G., Viero, C., Wang, Q., Mi, W., Su, X. D., Wagenknecht, T., Williams, A. J., Liu, Z. & Yin, C. C. (2009). *CLIC2-RyR1 interaction and structural characterization by cryo-electron microscopy. J. Mol. Biol.* **387**, 320–334.

Metlagel, Z., Kikkawa, Y. S. & Kikkawa, M. (2007). *Ruby-Helix: an implementation of helical image processing based on object-oriented scripting language. J. Struct. Biol.* **157**, 95–105.

Mikyas, Y., Makabi, M., Raval-Fernandes, S., Harrington, L., Kickhoefer, V. A., Rome, L. H. & Stewart, P. L. (2004). *Cryoelectron microscopy imaging of recombinant and tissue derived vaults: localization of the MVP N termini and VPARP. J. Mol. Biol.* **344**, 91–105.

Milazzo, A. C., Leblanc, P., Duttweiler, F., Jin, L., Bouwer, J. C., Peltier, S., Ellisman, M., Bieser, F., Matis, H. S., Wieman, H., Denes, P., Kleinfelder, S. & Xuong, N. H. (2005). *Active pixel sensor array as a detector for electron microscopy. Ultramicroscopy*, **104**, 152–159.

Milligan, R. A. (1996). *Protein–protein interactions in the rigor actomyosin complex. Proc. Natl Acad. Sci. USA*, **93**, 21–26.

Mindell, J. A. & Grigorieff, N. (2003). *Accurate determination of local defocus and specimen tilt in electron microscopy. J. Struct. Biol.* **142**, 334–347.

Miyazawa, A., Fujiyoshi, Y., Stowell, M. & Unwin, N. (1999). *Nicotinic acetylcholine receptor at 4.6 Å resolution: transverse tunnels in the channel wall. J. Mol. Biol.* **288**, 765–786.

Miyazawa, A., Fujiyoshi, Y. & Unwin, N. (2003). *Structure and gating mechanism of the acetylcholine receptor pore. Nature (London)*, **423**, 949–955.

Morgan, D. G. & DeRosier, D. (1992). *Processing images of helical structures: a new twist. Ultramicroscopy*, **46**, 263–285.

Morris, D. M. & Jensen, G. J. (2008). *Toward a biomechanical understanding of whole bacterial cells. Annu. Rev. Biochem.* **77**, 583–613.

Mouche, F., Zhu, Y., Pulokas, J., Potter, C. S. & Carragher, B. (2003). *Automated three-dimensional reconstruction of keyhole limpet hemocyanin type 1. J. Struct. Biol.* **144**, 301–312.

Muench, S. P., Huss, M., Song, C. F., Phillips, C., Wieczorek, H., Trinick, J. & Harrison, M. A. (2009). *Cryo-electron microscopy of the vacuolar ATPase motor reveals its mechanical and regulatory complexity. J. Mol. Biol.* **386**, 989–999.

Muller, S. A., Aebi, U. & Engel, A. (2008). *What transmission electron microscopes can visualize now and in the future. J. Struct. Biol.* **163**, 235–245.

Murata, K., Mitsuoka, K., Hirai, T., Walz, T., Agre, P., Heymann, J. B., Engel, A. & Fujiyoshi, Y. (2000). *Structural determinants of water permeation through aquaporin-1. Nature (London)*, **407**, 599–605.

Nagayama, K. & Danev, R. (2008). *Phase contrast electron microscopy: development of thin-film phase plates and biological applications. Philos. Trans. R. Soc. London Ser. B*, **363**, 2153–2162.

Navaza, J. (2003). *On the three-dimensional reconstruction of icosahedral particles. J. Struct. Biol.* **144**, 13–23.

Navaza, J., Lepault, J., Rey, F. A., Álvarez-Rúa, C. & Borge, J. (2002). *On the fitting of model electron densities into EM reconstructions: a reciprocal-space formulation*. Acta Cryst. D**58**, 1820–1825.

Nicastro, D., McIntosh, J. R. & Baumeister, W. (2005). *3D structure of eukaryotic flagella in a quiescent state revealed by cryo-electron tomography*. Proc. Natl Acad. Sci. USA, **102**, 15889–15894.

Nicastro, D., Schwartz, C., Pierson, J., Gaudette, R., Porter, M. E. & McIntosh, J. R. (2006). *The molecular architecture of axonemes revealed by cryoelectron tomography*. Science, **313**, 944–948.

Nickell, S., Beck, F., Korinek, A., Mihalache, O., Baumeister, W. & Plitzko, J. M. (2007). *Automated cryoelectron microscopy of 'single particles' applied to the 26S proteasome*. FEBS Lett. **581**, 2751–2756.

Nickell, S., Forster, F., Linaroudis, A., Net, W. D., Beck, F., Hegerl, R., Baumeister, W. & Plitzko, J. M. (2005). *TOM software toolbox: acquisition and analysis for electron tomography*. J. Struct. Biol. **149**, 227–234.

Nogales, E., Wolf, S. G. & Downing, K. H. (1998). *Structure of the $\alpha\beta$ tubulin dimer by electron crystallography*. Nature (London), **391**, 199–203.

Ogura, T. & Sato, C. (2006). *A fully automatic 3D reconstruction method using simulated annealing enables accurate posterioric angular assignment of protein projections*. J. Struct. Biol. **156**, 371–386.

Olins, D. E., Olins, A. L., Levy, H. A., Durfee, R. C., Margle, S. M., Tinnel, E. P. & Dover, S. D. (1983). *Electron microscopy tomography: transcription in three dimensions*. Science, **220**, 498–500.

Olson, N. H. & Baker, T. S. (1989). *Magnification calibration and the determination of spherical virus diameters using cryo-microscopy*. Ultramicroscopy, **30**, 281–298.

Orlova, A., Garner, E. C., Galkin, V. E., Heuser, J., Mullins, R. D. & Egelman, E. H. (2007). *The structure of bacterial ParM filaments*. Nat. Struct. Mol. Biol. **14**, 921–926.

Orzechowski, M. & Tama, F. (2008). *Flexible fitting of high-resolution X-ray structures into cryoelectron microscopy maps using biased molecular dynamics simulations*. Biophys. J. **95**, 5692–5705.

Ottmann, C., Marco, S., Jaspert, N., Marcon, C., Schauer, N., Weyand, M., Vandermeeren, C., Duby, G., Boutry, M., Wittinghofer, A., Rigaud, J. L. & Oecking, C. (2007). *Structure of a 14-3-3 coordinated hexamer of the plant plasma membrane H^+-ATPase by combining X-ray crystallography and electron cryomicroscopy*. Mol. Cell, **25**, 427–440.

Owen, C. H., Morgan, D. G. & DeRosier, D. J. (1996). *Image analysis of helical objects: the Brandeis helical package*. J. Struct. Biol. **116**, 167–175.

Penczek, P., Radermacher, M. & Frank, J. (1992). *Three-dimensional reconstruction of single particles embedded in ice*. Ultramicroscopy, **40**, 33–53.

Penczek, P. A., Grassucci, R. A. & Frank, J. (1994). *The ribosome at improved resolution: new techniques for merging and orientation refinement in 3D cryo-electron microscopy of biological particles*. Ultramicroscopy, **53**, 251–270.

Pettersen, E. F., Goddard, T. D., Huang, C. C., Couch, G. S., Greenblatt, D. M., Meng, E. C. & Ferrin, T. E. (2004). *UCSF Chimera – a visualization system for exploratory research and analysis*. J. Comput. Chem. **25**, 1605–1612.

Plaisier, J. R., Jiang, L. & Abrahams, J. P. (2007). *Cyclops: new modular software suite for cryo-EM*. J. Struct. Biol. **157**, 19–27.

Polyakov, A., Richter, C., Malhotra, A., Koulich, D., Borukhov, S. & Darst, S. A. (1998). *Visualization of the binding site for the transcript cleavage factor GreB on Escherichia coli RNA polymerase*. J. Mol. Biol. **281**, 465–473.

Pomfret, A. J., Rice, W. J. & Stokes, D. L. (2007). *Application of the iterative helical real-space reconstruction method to large membranous tubular crystals of P-type ATPases*. J. Struct. Biol. **157**, 106–116.

Potter, C. S., Chu, H., Frey, B., Green, C., Kisseberth, N., Madden, T. J., Miller, K. L., Nahrstedt, K., Pulokas, J., Reilein, A., Tcheng, D., Weber, D. & Carragher, B. (1999). *Leginon: a system for fully automated acquisition of 1000 electron micrographs a day*. Ultramicroscopy, **77**, 153–161.

Prust, C. J., Doerschuk, P. C., Lander, G. C. & Johnson, J. E. (2009). *Ab initio maximum likelihood reconstruction from cryo electron microscopy images of an infectious virion of the tailed bacteriophage P22 and maximum likelihood versions of Fourier shell correlation appropriate for measuring resolution of spherical or cylindrical objects*. J. Struct. Biol. **167**, 185–199.

Rabl, J., Smith, D. M., Yu, Y., Chang, S. C., Goldberg, A. L. & Cheng, Y. (2008). *Mechanism of gate opening in the 20S proteasome by the proteasomal ATPases*. Mol. Cell, **30**, 360–368.

Radermacher, M. (1988). *Three-dimensional reconstruction of single particles from random and nonrandom tilt series*. J. Electron Microsc. Tech. **9**, 359–394.

Radermacher, M. (1991). *Three-dimensional reconstruction of single particles in electron microscopy*. In *Image Analysis in Biology*, edited by D.-P. Hader, pp. 219–246. Boca Raton: CRC Press.

Radermacher, M. (1992). *Weighted back-projection methods*. In *Electron Tomography*, edited by J. Frank, pp. 91–115. New York: Plenum Press.

Radermacher, M. (1994). *Three-dimensional reconstruction from random projections: orientational alignment via Radon transforms*. Ultramicroscopy, **53**, 121–136.

Radermacher, M., Wagenknecht, T., Verschoor, A. & Frank, J. (1987). *Three-dimensional reconstructions from a single-exposure, random conical tilt series applied to the 50S ribosomal subunit of Escherichia coli*. J. Microsc. **146**, 113–136.

Ramey, V. H., Wang, H. W. & Nogales, E. (2009). *Ab initio reconstruction of helical samples with heterogeneity, disorder and coexisting symmetries*. J. Struct. Biol. **167**, 97–105.

Ranson, N. A., Clare, D. K., Farr, G. W., Houldershaw, D., Horwich, A. L. & Saibil, H. R. (2006). *Allosteric signaling of ATP hydrolysis in GroEL-GroES complexes*. Nat. Struct. Mol. Biol. **13**, 147–152.

Rayment, I., Holden, H. M., Whittaker, M., Yohn, C. B., Lorenz, M., Holmes, K. C. & Milligan, R. A. (1993). *Structure of the actin-myosin complex and its implications for muscle contraction*. Science, **261**, 58–65.

Reichow, S. L. & Gonen, T. (2009). *Lipid-protein interactions probed by electron crystallography*. Curr. Opin. Struct. Biol. **19**, 560–565.

Reimer, L. & Kohl, H. (2008). *Transmission Electron Microscopy: Physics of Image Formation*. New York: Springer Verlag.

Renault, L., Chou, H. T., Chiu, P. L., Hill, R. M., Zeng, X., Gipson, B., Zhang, Z. Y., Cheng, A., Unger, V. & Stahlberg, H. (2006). *Milestones in electron crystallography*. J. Comput. Aided Mol. Des. **20**, 519–527.

Roseman, A. M. (2000). *Docking structures of domains into maps from cryo-electron microscopy using local correlation*. Acta Cryst. D**56**, 1332–1340.

Roseman, A. M. (2003). *Particle finding in electron micrographs using a fast local correlation algorithm*. Ultramicroscopy, **94**, 225–236.

Rosenthal, P. B. & Henderson, R. (2003). *Optimal determination of particle orientation, absolute hand, and contrast loss in single-particle electron cryomicroscopy*. J. Mol. Biol. **333**, 721–745.

Rossmann, M. G., Bernal, R. & Pletnev, S. V. (2001). *Combining electron microscopic with X-ray crystallographic structures*. J. Struct. Biol. **136**, 190–200.

Rubinstein, J. L., Walker, J. E. & Henderson, R. (2003). *Structure of the mitochondrial ATP synthase by electron cryomicroscopy*. EMBO J. **22**, 6182–6192.

Sachse, C., Chen, J. Z., Coureux, P. D., Stroupe, M. E., Fandrich, M. & Grigorieff, N. (2007). *High-resolution electron microscopy of helical specimens: a fresh look at tobacco mosaic virus*. J. Mol. Biol. **371**, 812–835.

Salje, J., Zuber, B. & Lowe, J. (2009). *Electron cryomicroscopy of E. coli reveals filament bundles involved in plasmid DNA segregation*. Science, **323**, 509–512.

Sander, B., Golas, M. M. & Stark, H. (2005). *Advantages of CCD detectors for de novo three-dimensional structure determination in single-particle electron microscopy*. J. Struct. Biol. **151**, 92–105.

Sanner, M. F. (1999). *Python: A programming language for software integration and development*. J. Mol. Graph. Model. **17**, 57–61.

Sanner, M. F. (2005). *A component-based software environment for visualizing large macromolecular assemblies*. Structure, **13**, 447–462.

Schatz, M. & van Heel, M. (1990). *Invariant classification of molecular views in electron micrographs*. Ultramicroscopy, **32**, 255–264.

Schatz, M., Orlova, E. V., Dube, P., Jager, J. & van Heel, M. (1995). *Structure of Lumbricus terrestris hemoglobin at 30 Å resolution determined using angular reconstitution*. J. Struct. Biol. **114**, 28–40.

Scheres, S. H., Valle, M., Nunez, R., Sorzano, C. O., Marabini, R., Herman, G. T. & Carazo, J. M. (2005). *Maximum-likelihood multi-reference refinement for electron microscopy images*. J. Mol. Biol. **348**, 139–149.

Schmidt-Krey, I. (2007). *Electron crystallography of membrane proteins: two-dimensional crystallization and screening by electron microscopy*. Methods, **41**, 417–426.

Shacham, E., Sheehan, B. & Volkmann, N. (2007). *Density-based score for selecting near-native atomic models of unknown structures*. J. Struct. Biol. **158**, 188–195.

Shaikh, T. R., Barnard, D., Meng, X. & Wagenknecht, T. (2009). *Implementation of a flash-photolysis system for time-resolved cryo-electron microscopy*. J. Struct. Biol. **165**, 184–189.

Shaikh, T. R., Gao, H., Baxter, W. T., Asturias, F. J., Boisset, N., Leith, A. & Frank, J. (2008). *SPIDER image processing for single-particle reconstruction of biological macromolecules from electron micrographs*. Nat. Protoc. **3**, 1941–1974.

Sherman, M. B., Brink, J. & Chiu, W. (1996). *Performance of a slow-scan CCD camera for macromolecular imaging in a 400 kV electron cryomicroscope*. Micron, **27**, 129–139.

Shi, J., Williams, D. R. & Stewart, P. L. (2008). *A script-assisted microscopy (SAM) package to improve data acquisition rates on FEI Tecnai electron microscopes equipped with Gatan CCD cameras*. J. Struct. Biol. **164**, 166–169.

Short, J. M. (2004). *SLEUTH – a fast computer program for automatically detecting particles in electron microscope images*. J. Struct. Biol. **145**, 100–110.

Siegel, D. P. & Epand, R. M. (1997). *The mechanism of lamellar-to-inverted hexagonal phase transitions in phosphatidylethanolamine: implications for membrane fusion mechanisms*. Biophys. J. **73**, 3089–3111.

Siegel, D. P., Green, W. J. & Talmon, Y. (1994). *The mechanism of lamellar-to-inverted hexagonal phase transitions: a study using temperature-jump cryo-electron microscopy*. Biophys. J. **66**, 402–414.

Sorzano, C. O., Jonic, S., Nunez-Ramirez, R., Boisset, N. & Carazo, J. M. (2007). *Fast, robust, and accurate determination of transmission electron microscopy contrast transfer function*. J. Struct. Biol. **160**, 249–262.

Sorzano, C. O., Recarte, E., Alcorlo, M., Bilbao-Castro, J. R., San-Martin, C., Marabini, R. & Carazo, J. M. (2009). *Automatic particle selection from electron micrographs using machine learning techniques*. J. Struct. Biol. **167**, 252–260.

Sosa, H., Hoenger, A. & Milligan, R. A. (1997). *Three different approaches for calculating the three-dimensional structure of microtubules decorated with kinesin motor domains*. J. Struct. Biol. **118**, 149–158.

Sosa, H. & Milligan, R. A. (1996). *Three-dimensional structure of ncd-decorated microtubules obtained by a back-projection method*. J. Mol. Biol. **260**, 743–755.

Spence, J. C. H. (2009). *High-Resolution Electron Microscopy*. Oxford University Press.

Stagg, S. M., Lander, G. C., Pulokas, J., Fellmann, D., Cheng, A., Quispe, J. D., Mallick, S. P., Avila, R. M., Carragher, B. & Potter, C. S. (2006). *Automated cryoEM data acquisition and analysis of 284742 particles of GroEL*. J. Struct. Biol. **155**, 470–481.

Stagg, S. M., LaPointe, P., Razvi, A., Gurkan, C., Potter, C. S., Carragher, B. & Balch, W. E. (2008). *Structural basis for cargo regulation of COPII coat assembly*. Cell, **134**, 474–484.

Steven, A. C. & Baumeister, W. (2008). *The future is hybrid*. J. Struct. Biol. **163**, 186–195.

Stewart, M. (1988). *Computer image processing of electron micrographs of biological structures with helical symmetry*. J. Electron Microsc. Tech. **9**, 325–358.

Stewart, P. L., Chiu, C. Y., Huang, S., Muir, T., Zhao, Y., Chait, B., Mathias, P. & Nemerow, G. R. (1997). *Cryo-EM visualization of an exposed RGD epitope on adenovirus that escapes antibody neutralization*. EMBO J. **16**, 1189–1198.

Stewart, P. L., Fuller, S. D. & Burnett, R. M. (1993). *Difference imaging of adenovirus: bridging the resolution gap between X-ray crystallography and electron microscopy*. EMBO J. **12**, 2589–2599.

Subramaniam, S., Gerstein, M., Oesterhelt, D. & Henderson, R. (1993). *Electron diffraction analysis of structural changes in the photocycle of bacteriorhodopsin*. EMBO J. **12**, 1–18.

Suhre, K., Navaza, J. & Sanejouand, Y.-H. (2006). *NORMA: a tool for flexible fitting of high-resolution protein structures into low-resolution electron-microscopy-derived density maps*. Acta Cryst. D**62**, 1098–1100.

Suloway, C., Pulokas, J., Fellmann, D., Cheng, A., Guerra, F., Quispe, J., Stagg, S., Potter, C. S. & Carragher, B. (2005). *Automated molecular microscopy: the new Leginon system*. J. Struct. Biol. **151**, 41–60.

Suloway, C., Shi, J., Cheng, A., Pulokas, J., Carragher, B., Potter, C. S., Zheng, S. Q., Agard, D. A. & Jensen, G. J. (2009). *Fully automated, sequential tilt-series acquisition with Leginon*. J. Struct. Biol. **167**, 11–18.

Tama, F., Miyashita, O. & Brooks, C. L. III (2004*a*). *Flexible multi-scale fitting of atomic structures into low-resolution electron density maps with elastic network normal mode analysis*. J. Mol. Biol. **337**, 985–999.

Tama, F., Miyashita, O. & Brooks, C. L. III (2004*b*). *Normal mode based flexible fitting of high-resolution structure into low-resolution experimental data from cryo-EM*. J. Struct. Biol. **147**, 315–326.

Tama, F., Valle, M., Frank, J. & Brooks, C. L. III (2003). *Dynamic reorganization of the functionally active ribosome explored by normal mode analysis and cryo-electron microscopy*. Proc. Natl Acad. Sci. USA, **100**, 9319–9323.

Tan, R. K., Devkota, B. & Harvey, S. C. (2008). *YUP.SCX: coaxing atomic models into medium resolution electron density maps*. J. Struct. Biol. **163**, 163–174.

Tang, G., Peng, L., Baldwin, P. R., Mann, D. S., Jiang, W., Rees, I. & Ludtke, S. J. (2007). *EMAN2: an extensible image processing suite for electron microscopy*. J. Struct. Biol. **157**, 38–46.

Tang, J., Olson, N., Jardine, P. J., Grimes, S., Anderson, D. L. & Baker, T. S. (2008). *DNA poised for release in bacteriophage φ29*. Structure, **16**, 935–943.

Tao, Y., Olson, N. H., Xu, W., Anderson, D. L., Rossmann, M. G. & Baker, T. S. (1998). *Assembly of a tailed bacterial virus and its genome release studied in three dimensions*. Cell, **95**, 431–437.

Taylor, K. A. & Glaeser, R. M. (1974). *Electron diffraction of frozen, hydrated protein crystals*. Science, **186**, 1036–1037.

Taylor, K. A., Tang, J., Cheng, Y. & Winkler, H. (1997). *The use of electron tomography for structural analysis of disordered protein arrays*. J. Struct. Biol. **120**, 372–386.

Thuman-Commike, P. A. & Chiu, W. (1997). *Improved common line-based icosahedral particle image orientation estimation algorithms*. Ultramicroscopy, **68**, 231–255.

Thuman-Commike, P. A & Chiu, W. (2000). *Reconstruction principles of icosahedral virus structure determination using electron cryomicroscopy*. Micron, **31**, 687–711.

Tichelaar, W., Oostergetel, G. T., Haker, J., van Heel, M. G. & van Bruggen, E. F. J. (1980). *Scanning transmission electron microscopy of biological macromolecules*. Ultramicroscopy, **5**, 27–33.

Topf, M., Baker, M. L., John, B., Chiu, W. & Sali, A. (2005). *Structural characterization of components of protein assemblies by comparative modeling and electron cryo-microscopy*. J. Struct. Biol. **149**, 191–203.

Topf, M., Baker, M. L., Marti-Renom, M. A., Chiu, W. & Sali, A. (2006). *Refinement of protein structures by iterative comparative modeling and cryoEM density fitting*. J. Mol. Biol. **357**, 1655–1668.

Toyoshima, C. & Unwin, N. (1990). *Three-dimensional structure of the acetylcholine receptor by cryoelectron microscopy and helical image reconstruction*. J. Cell Biol. **111**, 2623–2635.

Toyoshima, C., Yonekura, K. & Sasabe, H. (1993). *Contrast transfer for frozen-hydrated specimens. II. Amplitude contrast at very low frequencies*. Ultramicroscopy, **48**, 165–176.

Trabuco, L. G., Villa, E., Mitra, K., Frank, J. & Schulten, K. (2008). *Flexible fitting of atomic structures into electron microscopy maps using molecular dynamics*. Structure, **16**, 673–683.

Trabuco, L. G., Villa, E., Schreiner, E., Harrison, C. B. & Schulten, K. (2009). *Molecular dynamics flexible fitting: a practical guide to combine cryo-electron microscopy and X-ray crystallography*. Methods, **49**, 174–180.

Trachtenberg, S. (1998). *A fast-freezing device with a retractable environmental chamber, suitable for kinetic cryo-electron microscopy studies*. J. Struct. Biol. **123**, 45–55.

Turchetta, R., Allport, P. P., Casse, G., Clark, A., Crooks, J., Evans, A., Fant, A., Faruqi, A. R., French, M. J. & Henderson, R. (2006). *CMOS monolithic active pixel sensors (MAPS): new 'eyes' for science*. Nucl. Instrum. Methods Phys. Res. A, **560**, 139–142.

Unger, V. M. (2000). *Assessment of electron crystallographic data obtained from two-dimensional crystals of biological specimens*. Acta Cryst. D**56**, 1259–1269.

Unser, M., Trus, B. L., Frank, J. & Steven, A. C. (1989). *The spectral signal-to-noise ratio resolution criterion: computational efficiency and statistical precision*. Ultramicroscopy, **30**, 429–434.

Unwin, N. (1993). *Nicotinic acetylcholine receptor at 9 Å resolution*. J. Mol. Biol. **229**, 1101–1124.

Unwin, N. (1995). *Acetylcholine receptor channel imaged in the open state*. Nature (London), **373**, 37–43.

Unwin, P. N. T. & Henderson, R. (1975). *Molecular structure determination by electron microscopy of unstained crystalline specimens*. J. Mol. Biol. **94**, 425–440.

Valpuesta, J. M., Carrascosa, J. L. & Henderson, R. (1994). *Analysis of electron microscope images and electron diffraction patterns of thin crystals of Φ29 connectors in ice. J. Mol. Biol.* **240**, 281–287.

Velazquez-Muriel, J. A. & Carazo, J. M. (2007). *Flexible fitting in 3D-EM with incomplete data on superfamily variability. J. Struct. Biol.* **158**, 165–181.

Velazquez-Muriel, J. A., Valle, M., Santamaria-Pang, A., Kakadiaris, I. A. & Carazo, J. M. (2006). *Flexible fitting in 3D-EM guided by the structural variability of protein superfamilies. Structure*, **14**, 1115–1126.

Venien-Bryan, C., Jonic, S., Skamnaki, V., Brown, N., Bischler, N., Oikonomakos, N. G., Boisset, N. & Johnson, L. N. (2009). *The structure of phosphorylase kinase holoenzyme at 9.9 Å resolution and location of the catalytic subunit and the substrate glycogen phosphorylase. Structure*, **17**, 117–127.

Villa, E., Sengupta, J., Trabuco, L. G., LeBarron, J., Baxter, W. T., Shaikh, T. R., Grassucci, R. A., Nissen, P., Ehrenberg, M., Schulten, K. & Frank, J. (2009). *Ribosome-induced changes in elongation factor Tu conformation control GTP hydrolysis. Proc. Natl Acad. Sci. USA*, **106**, 1063–1068.

Volkmann, N. (2002). *A novel three-dimensional variant of the watershed transform for segmentation of electron density maps. J. Struct. Biol.* **138**, 123–129.

Volkmann, N. & Hanein, D. (1999). *Quantitative fitting of atomic models into observed densities derived by electron microscopy. J. Struct. Biol.* **125**, 176–184.

Volkmann, N. & Hanein, D. (2003). *Docking of atomic models into reconstructions from electron microscopy. Methods Enzymol.* **374**, 204–225.

Voss, N. R., Yoshioka, C. K., Radermacher, M., Potter, C. S. & Carragher, B. (2009). *DoG Picker and TiltPicker: software tools to facilitate particle selection in single particle electron microscopy. J. Struct. Biol.* **166**, 205–213.

Wade, R. H. (1992). *A brief look at imaging and contrast transfer. Ultramicroscopy*, **46**, 145–156.

Wade, R. H. & Frank, J. (1977). *Electron microscope transfer functions for partially coherent axial illumination and chromatic defocus spread. Optik*, **49**, 81–92.

Walker, M., Zhang, X.-Z., Jiang, W., Trinick, J. & White, H. D. (1999). *Observation of transient disorder during myosin subfragment-1 binding to actin by stopped-flow fluorescence and millisecond time resolution electron cryomicroscopy: evidence that the start of the crossbridge power stroke in muscle has variable geometry. Proc. Natl Acad. Sci. USA*, **96**, 465–470.

Walz, J., Tamura, T., Tamura, N., Grimm, R., Baumeister, W. & Koster, A. J. (1997). *Tricorn protease exists as an icosahedral supermolecule in vivo. Mol. Cell*, **1**, 59–65.

Wang, G. J., Porta, C., Chen, Z., Baker, T. S. & Johnson, J. E. (1992). *Identification of a Fab interaction footprint site on an icosahedral virus by cryoelectron microscopy and X-ray crystallography. Nature (London)*, **355**, 275–278.

Wang, H. W. & Nogales, E. (2005). *An iterative Fourier–Bessel algorithm for reconstruction of helical structures with severe Bessel overlap. J. Struct. Biol.* **149**, 65–78.

Wang, M. C., Collins, R. F., Ford, R. C., Berrow, N. S., Dolphin, A. C. & Kitmitto, A. (2004). *The three-dimensional structure of the cardiac L-type voltage-gated calcium channel: comparison with the skeletal muscle form reveals a common architectural motif. J. Biol. Chem.* **279**, 7159–7168.

Wang, Y. A., Yu, X., Overman, S., Tsuboi, M., Thomas, G. J. Jr & Egelman, E. H. (2006). *The structure of a filamentous bacteriophage. J. Mol. Biol.* **361**, 209–215.

Weik, M., Ravelli, R. B., Kryger, G., McSweeney, S., Raves, M. L., Harel, M., Gros, P., Silman, I., Kroon, J. & Sussman, J. L. (2000). *Specific chemical and structural damage to proteins produced by synchrotron radiation. Proc. Natl Acad. Sci. USA*, **97**, 623–628.

White, H. D., Thirumurugan, K., Walker, M. L. & Trinick, J. (2003). *A second generation apparatus for time-resolved electron cryomicroscopy using stepper motors and electrospray. J. Struct. Biol.* **144**, 246–252.

White, H. D., Walker, M. L. & Trinick, J. (1998). *A computer-controlled spraying-freezing apparatus for millisecond time-resolution electron cryomicroscopy. J. Struct. Biol.* **121**, 306–313.

Whittaker, M., Carragher, B. O. & Milligan, R. A. (1995). *PHOELIX: a package for semi-automated helical reconstruction. Ultramicroscopy*, **58**, 245–259.

Wilson-Kubalek, E. M., Brown, R. E., Celia, H. & Milligan, R. A. (1998). *Lipid nanotubes as substrates for helical crystallization of macromolecules. Proc. Natl Acad. Sci. USA*, **95**, 8040–8045.

Winkelmann, D. A., Baker, T. S. & Rayment, I. (1991). *Three-dimensional structure of myosin subfragment-1 from electron microscopy of sectioned crystals. J. Cell Biol.* **114**, 701–713.

Winkler, H. & Taylor, K. A. (1994). *3D reconstruction by combining data from sections cut oblique to different unit cell axes. Ultramicroscopy*, **55**, 357–371.

Winkler, H. & Taylor, K. A. (1996). *Software for 3-D reconstruction from images of oblique sections through 3-D crystals. J. Struct. Biol.* **116**, 241–247.

Woolford, D., Ericksson, G., Rothnagel, R., Muller, D., Landsberg, M. J., Pantelic, R. S., McDowall, A., Pailthorpe, B., Young, P. R., Hankamer, B. & Banks, J. (2007). *SwarmPS: rapid, semi-automated single particle selection software. J. Struct. Biol.* **157**, 174–188.

Wriggers, W. & Birmanns, S. (2001). *Using Situs for flexible and rigid-body fitting of multiresolution single-molecule data. J. Struct. Biol.* **133**, 193–202.

Wriggers, W. & Chacon, P. (2001). *Modeling tricks and fitting techniques for multiresolution structures. Structure*, **9**, 779–788.

Wriggers, W., Milligan, R. A. & McCammon, J. A. (1999). *Situs: a package for docking crystal structures into low-resolution maps from electron microscopy. J. Struct. Biol.* **125**, 185–195.

Xuong, N. H., Jin, L., Kleinfelder, S., Li, S., Leblanc, P., Duttweiler, F., Bouwer, J. C., Peltier, S. T., Milazzo, A. C. & Ellisman, M. (2007). *Future directions for camera systems in electron microscopy. Methods Cell Biol.* **79**, 721–739.

Yan, X., Dryden, K. A., Tang, J. & Baker, T. S. (2007). *Ab initio random model method facilitates 3D reconstruction of icosahedral particles. J. Struct. Biol.* **157**, 211–225.

Yan, X., Sinkovits, R. S. & Baker, T. S. (2007). *AUTO3DEM – an automated and high throughput program for image reconstruction of icosahedral particles. J. Struct. Biol.* **157**, 73–82.

Yang, C., Penczek, P. A., Leith, A., Asturias, F. J., Ng, E. G., Glaeser, R. M. & Frank, J. (2007). *The parallelization of SPIDER on distributed-memory computers using MPI. J. Struct. Biol.* **157**, 240–249.

Yeager, M., Unger, V. M. & Mitra, A. K. (1999). *Three-dimensional structure of membrane proteins determined by two-dimensional crystallization, electron cryomicroscopy, and image analysis. Methods Enzymol.* **294**, 135–180.

Yonekura, K., Braunfeld, M. B., Maki-Yonekura, S. & Agard, D. A. (2006). *Electron energy filtering significantly improves amplitude contrast of frozen-hydrated protein at 300kV. J. Struct. Biol.* **156**, 524–536.

Yonekura, K., Maki-Yonekura, S. & Namba, K. (2003). *Complete atomic model of the bacterial flagellar filament by electron cryomicroscopy. Nature (London)*, **424**, 643–650.

Yonekura, K., Toyoshima, C., Maki-Yonekura, S. & Namba, K. (2003). *GUI programs for processing individual images in early stages of helical image reconstruction – for high-resolution structure analysis. J. Struct. Biol.* **144**, 184–194.

Yoshimura, H., Matsumoto, M., Endo, S. & Nagayama, K. (1990). *Two-dimensional crystallization of proteins on mercury. Ultramicroscopy*, **32**, 265–274.

Yoshioka, C., Pulokas, J., Fellmann, D., Potter, C. S., Milligan, R. A. & Carragher, B. (2007). *Automation of random conical tilt and orthogonal tilt data collection using feature-based correlation. J. Struct. Biol.* **159**, 335–346.

Yu, X., Hiromasa, Y., Tsen, H., Stoops, J. K., Roche, T. E. & Zhou, Z. H. (2008). *Structures of the human pyruvate dehydrogenase complex cores: a highly conserved catalytic center with flexible N-terminal domains. Structure*, **16**, 104–114.

Yu, X., Jin, L. & Zhou, Z. H. (2008). *3.88 Å structure of cytoplasmic polyhedrosis virus by cryo-electron microscopy. Nature (London)*, **453**, 415–419.

Yu, X., Wang, L., Acehan, D., Wang, X. & Akey, C. W. (2006). *Three-dimensional structure of a double apoptosome formed by the Drosophila Apaf-1 related killer. J. Mol. Biol.* **355**, 577–589.

Zanetti, G., Briggs, J. A., Grunewald, K., Sattentau, Q. J. & Fuller, S. D. (2006). *Cryo-electron tomographic structure of an immunodeficiency virus envelope complex in situ. PLoS Pathog.* **2**, 790–797.

Zanetti, G., Riches, J. D., Fuller, S. D. & Briggs, J. A. (2009). *Contrast transfer function correction applied to cryo-electron tomography and sub-tomogram averaging. J. Struct. Biol.* **168**, 305–312.

Zemlin, F. (1992). *Desired features of a cryoelectron microscope for the electron crystallography of biological material. Ultramicroscopy*, **46**, 25–32.

Zemlin, F., Beckmann, E. & van der Mast, K. D. (1996). *A 200 kV electron microscope with Schottky field emitter and a helium-cooled superconducting objective lens. Ultramicroscopy*, **63**, 227–238.

Zeng, X., Gipson, B., Zheng, Z. Y., Renault, L. & Stahlberg, H. (2007). *Automatic lattice determination for two-dimensional crystal images. J. Struct. Biol.* **160**, 353–361.

Zhang, J., Nakamura, N., Shimizu, Y., Liang, N., Liu, X., Jakana, J., Marsh, M. P., Booth, C. R., Shinkawa, T., Nakata, M. & Chiu, W. (2009). *JADAS: a customizable automated data acquisition system and its application to ice-embedded single particles. J. Struct. Biol.* **165**, 1–9.

Zhang, P., Borgnia, M. J., Mooney, P., Shi, D., Pan, M., O'Herron, P., Mao, A., Brogan, D., Milne, J. L. & Subramaniam, S. (2003). *Automated image acquisition and processing using a new generation of 4K × 4K CCD cameras for cryo electron microscopic studies of macromolecular assemblies. J. Struct. Biol.* **143**, 135–144.

Zhang, X., Settembre, E., Xu, C., Dormitzer, P. R., Bellamy, R., Harrison, S. C. & Grigorieff, N. (2008). *Near-atomic resolution using electron cryomicroscopy and single-particle reconstruction. Proc. Natl Acad. Sci. USA*, **105**, 1867–1872.

Zheng, Q. S., Braunfeld, M. B., Sedat, J. W. & Agard, D. A. (2004). *An improved strategy for automated electron microscopic tomography. J. Struct. Biol.* **147**, 91–101.

Zheng, S. Q., Keszthelyi, B., Branlund, E., Lyle, J. M., Braunfeld, M. B., Sedat, J. W. & Agard, D. A. (2007). *UCSF tomography: an integrated software suite for real-time electron microscopic tomographic data collection, alignment, and reconstruction. J. Struct. Biol.* **157**, 138–147.

Zheng, S. Q., Kollman, J. M., Braunfeld, M. B., Sedat, J. W. & Agard, D. A. (2006). *Automated acquisition of electron microscopic random conical tilt sets. J. Struct. Biol.* **157**, 148–155.

Zhou, Z. H. (2008). *Towards atomic resolution structural determination by single-particle cryo-electron microscopy. Curr. Opin. Struct. Biol.* **18**, 218–228.

Zhou, Z. H., Baker, M. L., Jiang, W., Dougherty, M., Jakana, J., Dong, G., Lu, G. & Chiu, W. (2001). *Electron cryomicroscopy and bioinformatics suggest protein fold models for rice dwarf virus. Nat. Struct. Biol.* **8**, 868–873.

Zhou, Z. H. & Chiu, W. (1993). *Prospects for using an IVEM with a FEG for imaging macromolecules towards atomic resolution. Ultramicroscopy*, **49**, 407–416.

Zhou, Z. H., Chiu, W., Haskell, K., Spears, H. J., Jakana, J., Rixon, F. J. & Scott, L. R. (1998). *Refinement of herpesvirus B-capsid structure on parallel supercomputers. Biophys. J.* **74**, 576–588.

Zhou, Z. H., Hardt, S., Wang, B., Sherman, M. B., Jakana, J. & Chiu, W. (1996). *CTF determination of images of ice-embedded single particles using a graphics interface. J. Struct. Biol.* **116**, 216–222.

Zhu, P., Winkler, H., Chertova, E., Taylor, K. A. & Roux, K. H. (2008). *Cryoelectron tomography of HIV-1 envelope spikes: further evidence for tripod-like legs. PLoS Pathog.* **4**, e1000203.

Zhu, Y., Carragher, B., Glaeser, R. M., Fellmann, D., Bajaj, C., Bern, M., Mouche, F., de Haas, F., Hall, R. J., Kriegman, D. J., Ludtke, S. J., Mallick, S. P., Penczek, P. A., Roseman, A. M., Sigworth, F. J., Volkmann, N. & Potter, C. S. (2004). *Automatic particle selection: results of a comparative study. J. Struct. Biol.* **145**, 3–14.

Ziese, U., Geerts, W. J., van der Krift, T. P., Verkleij, A. J. & Koster, A. J. (2003). *Correction of autofocusing errors due to specimen tilt for automated electron tomography. J. Microsc.* **211**, 179–185.

Ziese, U., Janssen, A. H., Murk, J. L., Geerts, W. J., van der Krift, T., Verkleij, A. J. & Koster, A. J. (2002). *Automated high-throughput electron tomography by pre-calibration of image shifts. J. Microsc.* **205**, 187–200.

Zuber, B., Chami, M., Houssin, C., Dubochet, J., Griffiths, G. & Daffe, M. (2008). *Direct visualization of the outer membrane of mycobacteria and corynebacteria in their native state. J. Bacteriol.* **190**, 5672–5680.

Zuber, B., Nikonenko, I., Klauser, P., Muller, D. & Dubochet, J. (2005). *The mammalian central nervous synaptic cleft contains a high density of periodically organized complexes. Proc. Natl Acad. Sci. USA*, **102**, 19192–19197.

references